CEAS Space Journal (2025) 17:31–54
https://doi.org/10.1007/s12567-024-00544-0

ORIGINAL PAPER

Flight control design for a hypersonic waverider configuration: A non-linear model following control approach

Johannes Autenrieb[1] · **Nicolas Fezans**[1]

Received: 28 March 2023 / Revised: 24 January 2024 / Accepted: 14 February 2024 / Published online: 25 April 2024

Abstract

DLR is currently investigating the potential of hypersonic flight systems in the context of different mission scenarios. One configuration type of higher interest for civil and military purposes is the hypersonic glide vehicle (HGV). Such HGVs operate over broad flight envelopes and pose complex flight dynamic characteristics. This article presents DLR's generic hypersonic glide vehicle 2 (GHVG-2) and proposes an integrated non-linear flight control architecture that is based on the idea of the non-linear dynamic inversion and non-linear model following control methodologies. The proposed control scheme is designed to sufficiently and robustly handle the system dynamics of the over-actuated flight vehicle. The approach is first discussed, and the performance of the suggested control laws is later investigated via simulations of a high-fidelity non-linear flight dynamic model in the nominal case and under the presence of parametric uncertainties. The presented results demonstrate that the proposed NMFC approach provides benefits for the robust control of the regarded hypersonic system.

Keywords Non-linear flight control · Non-linear dynamic inversion · Non-linear model following control · Hypersonic glide vehicles · Waverider · Flight mechanics

Abbreviations

CA	Control allocation
CFD	Computational fluid dynamics
DLR	Deutsches Zentrum für Luft- und Raumfahrt (German Aerospace Center)
FCS	Flight control system
GHGV-2	Generic hypersonic glide vehicle 2
GNC	Guidance, navigation and control
HGV	Hypersonic glide vehicle
INDI	Incremental Non-linear Dynamic Inversion
ISA	International Standard Atmosphere
NDI	Non-linear dynamic inversion
NMFC	Non-linear model following control
PCH	Pseudo control hedging
RM	Reference model
SAS	Stability augmentation system
TPS	Thermal protection system
WGS84	World Geodetic System 1984

Symbols

α	Angle of attack in rad
β	Side-slip angle in rad
C_i	Aerodynamic coefficient
χ	Flight path azimuth angle in rad
D	Damping ratio
δ_i	Control surface deflection in rad
γ	Flight path angle in rad
H	Altitude in m
I	Moment of inertia in kgm^2
λ	Longitude in rad
L,M,N	External moments in the body axes in Nm
m	Mass in kg
Ma	Mach number
μ	Flight path bank angle in rad
ω	Natural frequency in rad/s
p,q,r	Roll, pitch, yaw rate in the body axes in rad/s
ϕ	Latitude in rad
ρ	Freestream density in kg/m^3
S	Aerodynamic reference area in m^2
u,v,w	Velocities in the body axes in m/s
V	Flight speed in m/s

✉ Johannes Autenrieb
johannes.autenrieb@dlr.de

Nicolas Fezans
nicolas.fezans@dlr.de

[1] Institute of Flight Systems, Department of Flight Dynamics and Simulation, DLR, German Aerospace Center, Lilienthalplatz 7, Braunschweig 38108, Lower-Saxony, Germany

X,Y,Z	External forces in the body axes in N
x,y,z	Distances in the body axes in m

Subscripts

a	Aerodynamic frame
c	Command
cp	Centre of pressure
cg	Centre of gravity
d	Desired attitude angles signal coming from the guidance loop
K	Motion with respect to the inertial frame
r	Reference

Superscripts

(k)	K-th time derivative

Accents

$\dot{}$	Time derivative
$\hat{}$	Measured or estimated value

1 Introduction

In the last years, hypersonic glide vehicles (HGVs) have been increasingly the subject of research and development efforts of both academia and industry [3]. This emerging class of vehicle possesses the ability to be applied in the civil and military sector [4]. DLR is currently studying the physical limitations and performance of autonomous hypersonic flight systems in different mission scenarios. Well-designed autopilots are compulsory for all autonomously operating flight vehicles. They stabilise the vehicle and ensure good tracking of an online or offline computed trajectory to reach the desired location. Particularly for the application in hypersonic vehicles, the implemented guidance and control systems need to adequately and robustly handle the complex physical effects over large flight envelopes, under the presence of model uncertainties and fairly inaccurate model assumptions. One promising control approach which is naturally able to handle highly non-linear systems is the non-linear dynamic inversion (NDI) control methodology.

NDI has been successfully applied and tested for flight control systems (FCSs) of different aerial vehicle classes in recent years. In [5], the authors successfully applied cascaded NDI feedback controllers for the autonomous attitude control of a hypersonic re-entry vehicle, in [6] for the control augmentation system of a supermaneuverable aircraft and in [7] for the flight control of spin-stabilized guided projectiles. Both discussed approaches use a time-scale separation for improved robustness of the continuous feedback linearisation scheme [8]. Despite the major benefits, NDI-based control methods come also with drawbacks. In particular, the model-based methodology can be sensitive to mathematical model uncertainties, which could lead to significant performance degradation and even closed-loop instabilities, due to inversion errors [9].

Several approaches have been reported in the literature where an incremental formulation of the non-linear dynamic inversion control (INDI) were proposed to increase the controllers robustness towards parametric model uncertainties [10–13]. Even though the said approaches show promising results, INDI-based concepts, in the case of attitude control, rely on correct and instantaneous measurements of the angular acceleration and control effector states. This is not always given and hence the control system could be exposed to instability problems if these signals are not directly measurable and estimates have significant noise, delays, or biases [14]. To cope with problems related to imperfect sensor measurements, complementary filters can be used to fuse model-based information and sensor measurements, keeping the beneficial characteristics of both signals, cf. [15, 16]. The problem of model uncertainties in the context of NDI-based control approaches can be addressed, as shown in [17, 18], by augmenting the baseline controllers with adaptive modules, that are capable of compensating the effect of these uncertainties.

Even though all the approaches using INDI or adaptive control show promising results, the established control systems mutually rely on the implemented linear feedback controllers for good tracking performance and stability augmentation. Such a control structure makes it tedious to tune the controllers and favour decreased robustness properties of the closed-loop system. This paper proposes a flight control architecture that uses the fundamental ideas presented in [5, 6] for non-linear feedback control but enhances the structures with a feedforward signal based on the idea of a non-linear model following control (NMFC) approach [19]. The paper's main contribution is the presentation and discussion of the NMFC methodology, which combines cascaded and non-cascaded NDI-based control schemes to increase overall robustness of a baseline controller by fundamentally separating the command tracking task from the stability augmentation task of the controllers. This controller can be easily enhanced later, using an incremental formulation as shown in [15], or augmented using adaptive controllers as shown in [18].

The remainder of the article is organised as follows. Section 2 gives an overview of the generic hypersonic glide vehicle 2 (GHGV-2) and the non-linear mathematical modelling of the vehicle. Further, the fundamental idea of non-linear dynamic inversion is introduced in Sect. 3, and the proposed non-linear flight control system is discussed in Sect. 4. Finally, in Sect. 5, the robustness and performance of the system are analyzed based on the developed 6-dof non-linear simulation.

2 Hypersonic glide vehicle modeling

2.1 The DLR GHGV-2 Concept

The considered GHGV-2 configuration has been designed by a multi-disciplinary development group of DLR. It was developed to investigate hypersonic glide vehicles' physical capabilities, limitations, and future impact on civil and military operations. The developed vehicle is shown in Fig. 1. The sectional view of Fig. 1b shows some of the most relevant sub-systems for the present work, such as the thermal protection system (TPS), guidance, navigation & control system (GNC), battery system, and actuation system. The flight vehicle is based on the waverider concept and is designed to improve lift-to-drag ratios within operations in high Mach number regimes [20].

Figure 2 illustrates the vertical trajectory of a possible mission profile for the GHGV-2. For the investigated use case, it is expected that the GHGV-2 is launched with a multi-stage rocket booster. After the ignition and acceleration of the rocket, the hypersonic vehicle decouples from the launch vehicle at an altitude of approximately 100 km, from where it initiates a parabolic re-entry phase. The vehicle is equipped with thrusters to control the vehicle in altitudes in which no sufficient aerodynamical control authority can be guaranteed. Once sufficient dynamic pressure is reached during the re-entry, the four available aerodynamical control surfaces (two on the upper and two on the lower side) are used to control the vehicle. After the re-entry phase is completed, the HGV attempts to follow a specific flight path angle profile, which allows it to remain at its maximum lift-to-drag ratio while flying toward its target location.

(a) External view on the GHGV-2

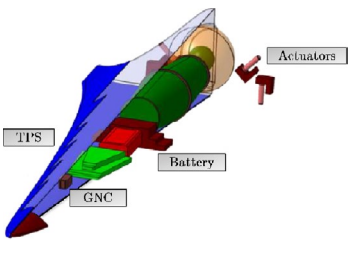

(b) Sectional view of the GHGV-2

Fig. 1 The DLR Generic Hypersonic Glide Vehicle Concept [20]

An integrated guidance, navigation, and control (GNC) system steers the vehicle along a desired trajectory to obtain the needed maneuvers. Figure 3 shows a conceptual architecture of the overall GNC system of the GHGV-2. Before the start of a mission, the trajectory for the vehicle is computed using optimisation-based approaches such as shown in [21]. These trajectories are computed such that physical constraints (e.g., thermal loads) and operational constraints (e.g., no-fly zones) are respected. During the mission, a trajectory tracking algorithm uses the vehicle's current position and the pre-computed waypoint information to calculate the required flight path angle γ_d and azimuth angle χ_d. The demanded flight path and azimuth angle are then fed into a non-linear flight path controller that generates the required aerodynamic angles $(\mu_d, \alpha_d, \beta_d)$, later used by the non-linear attitude control system, which generates a desired angular acceleration command vector $\vec{\nu}_d = (\dot{p}_d, \dot{q}_d, \dot{r}_d)^T$. The angular acceleration command vector is then fed into a control allocation (CA) system to optimally compute the control input vector for the over-actuated vehicle. Even though all presented sub-modules have a substantial internal dependency on each other, the discussions within the here presented work will focus on the "non-linear attitude control" and "control allocation" modules.

2.2 Aerodynamics

The aerodynamic database considers static and dynamic aerodynamical effects modeled as static and dynamic derivative coefficients. Each of the coefficients and derivatives are a function of the Mach number Ma, the altitude H, the angle of attack α and the angle of sideslip β (see Eq. 1- 6).

$$X = \frac{\rho}{2} V^2 S \left[C_X(\alpha, \beta, \mathrm{Ma}, \mathrm{H}) + C_{X,q}(\alpha, \beta, \mathrm{Ma}, \mathrm{H}) \frac{q\, l_r}{2\, V} \right] \tag{1}$$

$$\begin{aligned} Y = &\frac{\rho}{2} V^2 S \left[C_Y(\alpha, \beta, \mathrm{Ma}, \mathrm{H}) + C_{Y,r}(\alpha, \beta, \mathrm{Ma}, \mathrm{H}) \frac{r\, l_r}{2\, V} \right. \\ &\left. + C_{Y\dot{\beta}}(\alpha, \beta, \mathrm{Ma}, \mathrm{H}) \frac{\dot{\beta}\, l_r}{2\, V} \right] \end{aligned} \tag{2}$$

$$\begin{aligned} Z = &\frac{\rho}{2} V^2 S \left[C_Z(\alpha, \beta, \mathrm{Ma}, \mathrm{H}) + C_{Z,q}(\alpha, \beta, \mathrm{Ma}, \mathrm{H}) \frac{q\, l_r}{2\, V} \right. \\ &\left. + C_{Z,\dot{\alpha}}(\alpha, \beta, \mathrm{Ma}, \mathrm{H}) \frac{\dot{\alpha}\, l_r}{2\, V} \right] \end{aligned} \tag{3}$$

$$\begin{aligned} L = &\frac{\rho}{2} V^2 S \left[C_l(\alpha, \beta, \mathrm{Ma}, \mathrm{H}) + C_{l,p}(\alpha, \beta, \mathrm{Ma}, \mathrm{H}) \frac{q\, l_r}{2\, V} \right] \\ &- Y \Delta z_{cp-cg} - Z \Delta y_{cp-cg} \end{aligned} \tag{4}$$

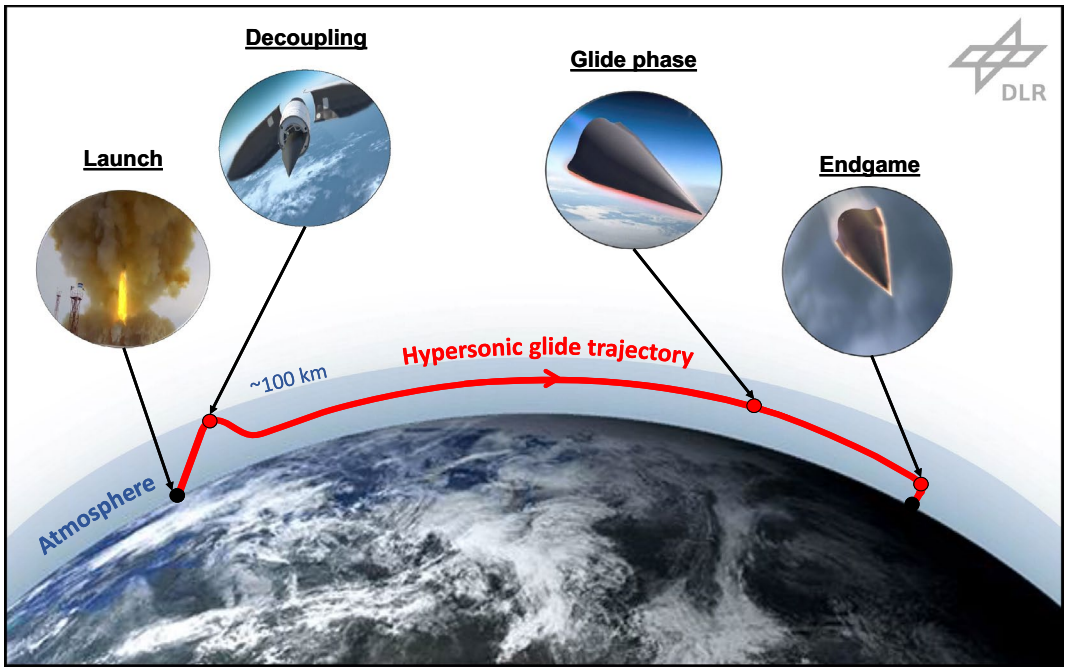

Fig. 2 Illustration of an exemplary mission of a hypersonic glide vehicle

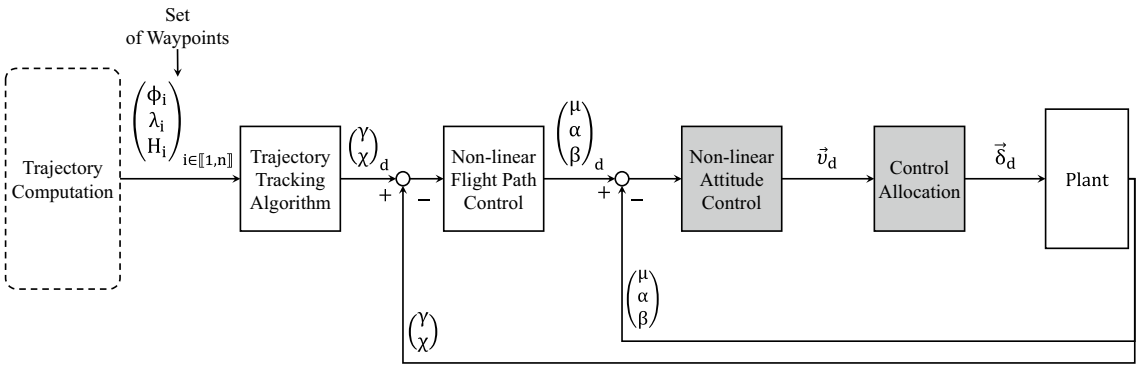

Fig. 3 Overview of the integrated overall guidance and control architecture of the GHGV-2 [22]

$$M = \frac{\rho}{2}V^2 S\left[C_M(\alpha,\beta,\mathrm{Ma},\mathrm{H}) + C_{M,q}(\alpha,\beta,\mathrm{Ma},\mathrm{H})\frac{q l_r}{2V} + C_{M\dot{\alpha}}(\alpha,\beta,\mathrm{Ma},\mathrm{H})\frac{\dot{\alpha}\, l_r}{2\,V}\right] - Z\Delta x_{cp-cg} + X\Delta z_{cp-cg} \tag{5}$$

$$N = \frac{\rho}{2}V^2 S\left[C_N(\alpha,\beta,\mathrm{Ma},\mathrm{H}) + C_{N,r}(\alpha,\beta,\mathrm{Ma},\mathrm{H})\frac{r l_r}{2V} + C_{N,\dot{\beta}}(\alpha,\beta,\mathrm{Ma},\mathrm{H})\frac{\dot{\beta}\, l_r}{2\,V}\right] + X\Delta y_{cp-cg} + Y\Delta x_{cp-cg} \tag{6}$$

The static aerodynamic coefficients have been calculated by computational fluid dynamics (CFD) using the DLR TAU code [23, 24]. Within the CFD analysis, around 800 inviscid calculations have been performed in the Mach number range from 0.6 to 12.5, for angles of attack between −6° and 15°, for angles of sideslip between 0° and 3°. The rudder deflection angles of the upper and lower flaps have been varied within the full deflection range of 0°and 20° with regards to the respective coordinate system of the corresponding control surface. The environmental conditions for each Mach

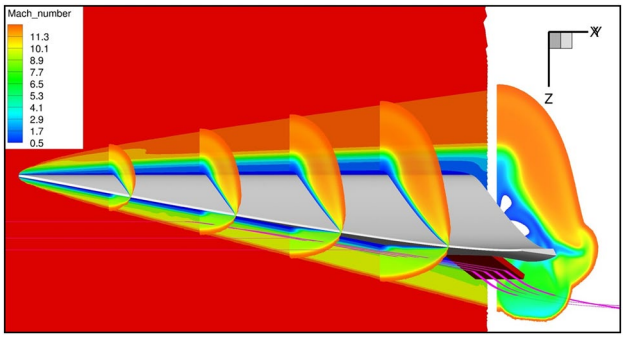

Fig. 4 Example image of CFD calculated Mach number distribution around the GHGV-2 at Mach number 12.5 [20]

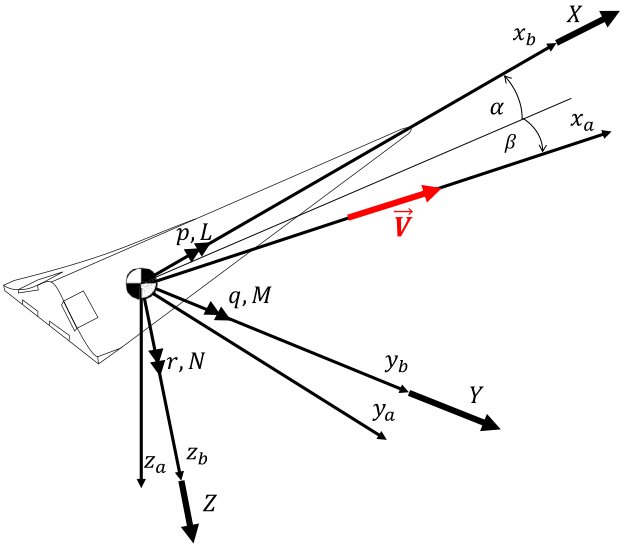

Fig. 5 Sketch of external forces and moments acting on the GHGV-2 concept

number were based on the standard atmospheric conditions at a specific altitude taken from a pre-determined trajectory (i.e., no further Reynolds number variation was performed). In order to take viscous effects into account, fully viscous Reynolds-Averaged Navier–Stokes simulations have been performed for selected trajectory points. Those calculations were then used to calculate a viscous correction model that was applied to all data points. The corrected coefficients are then implemented as a lookup table into the non-linear flight dynamics model. As an example, Fig. 4 shows the CFD calculated Mach number distribution around the GHGV-2 at Mach number 12.5.

2.3 Non-linear flight dynamics

The modeled non-linear flight dynamics of the GHGV-2 are based on classical Newtonian mechanics, in which the vehicle is assumed as a rigid body. Figure 5 displays the components of the total external forces X, Y, Z and the total external moments L, M, N expressed in the body-fixed frame of the vehicle. For the investigated case, only the aerodynamic and gravitational forces and moments are considered relevant during the regarded reentry and glide phases since hypersonic glide vehicles are commonly unpropelled during those mission stages. Centrifugal and Coriolis forces that are originating from motions within a moving reference system (consideration of Earth's rotation) are additionally computed and taken into account as external forces in the body-fixed frame. Atmospheric effects have been modeled using the International Standard Atmosphere (ISA) [25].

The generalised equations of motion for the modelled HGV are presented for the translational motion in Eq. (7) and for the rotational motion in Eq. (8).

$$\begin{bmatrix} X \\ Y \\ Z \end{bmatrix} = m \begin{bmatrix} \dot{u}_K \\ \dot{v}_K \\ \dot{w}_K \end{bmatrix} + m \begin{bmatrix} p_K \\ q_K \\ r_K \end{bmatrix} \times \begin{bmatrix} u_K \\ v_K \\ w_K \end{bmatrix} \tag{7}$$

$$\begin{bmatrix} L \\ M \\ N \end{bmatrix} = I \begin{bmatrix} \dot{p}_K \\ \dot{q}_K \\ \dot{r}_K \end{bmatrix} + \begin{bmatrix} p_K \\ q_K \\ r_K \end{bmatrix} \times I \begin{bmatrix} p_K \\ q_K \\ r_K \end{bmatrix} \tag{8}$$

The kinematic relationship allowing expressing the time derivatives $(\dot{\mu}_K, \dot{\alpha}_K, \dot{\beta}_K)$ of the flight-path bank angle μ_K, the angle of attack α_K and the sideslip angle β_K as a function of the body-fixed rotational rates p_K, q_K, r_K and the time derivatives $(\dot{\gamma}, \dot{\chi})$ of the flight path angle γ and χ reads [26, 27]:

$$\begin{aligned} \begin{bmatrix} \dot{\mu}_K \\ \dot{\alpha}_K \\ \dot{\beta}_K \end{bmatrix} &= T_1 \begin{bmatrix} p_K \\ q_K \\ r_K \end{bmatrix} + T_2 \begin{bmatrix} \dot{\gamma} \\ \dot{\chi} \end{bmatrix} \\ &= \begin{bmatrix} \frac{\cos\alpha_K}{\cos\beta_K} & 0 & \frac{\sin\alpha_K}{\cos\beta_K} \\ -\cos\alpha_K \tan\beta_K & 1 & -\sin\alpha_K \tan\beta_K \\ \sin\alpha_K & 0 & -\cos\alpha_K \end{bmatrix} \begin{bmatrix} p_K \\ q_K \\ r_K \end{bmatrix} \\ &\quad + \begin{bmatrix} \cos\mu_K \tan\beta_K & \sin\gamma + \sin\mu \tan\beta_K \cos\gamma \\ -\frac{\cos\mu_K}{\cos\beta_K} & -\frac{\sin\mu_K \cos\gamma}{\cos\beta_K} \\ -\sin\mu_K & \cos\mu_K \cos\gamma \end{bmatrix} \begin{bmatrix} \dot{\gamma} \\ \dot{\chi} \end{bmatrix} \end{aligned} \tag{9}$$

Equation (9) constitutes a kinematic relationship between various reference frames. In this equation, the rotational rates p_K, q_K, and r_K are obtained from the integration of the moment equation of Eq. (8). The time derivatives $\dot{\gamma}$ and $\dot{\chi}$ of the flight path and track angles γ and χ result from the accelerations of the vehicle and can therefore be expressed

as functions of the external forces, once expressed in the flight path frame, divided by the translational momentum $m\,V$ (see for instance [6]). The relevant external forces are the weight W, the aerodynamic lift force L_a, and the aerodynamic side force Y_a.

$$\begin{aligned}\begin{bmatrix}\dot{\mu}_K\\ \dot{\alpha}_K\\ \dot{\beta}_K\end{bmatrix} &= T_1\begin{bmatrix}p_K\\ q_K\\ r_K\end{bmatrix} + \left(\frac{1}{m\,V}\right)T_3\begin{bmatrix}-W\\ L_a\\ Y_a\end{bmatrix}\\ &= \begin{bmatrix}\frac{\cos\alpha_K}{\cos\beta_K} & 0 & \frac{\sin\alpha_K}{\cos\beta_K}\\ -\cos\alpha_K\tan\beta_K & 1 & -\sin\alpha_K\tan\beta_K\\ \sin\alpha_K & 0 & -\cos\alpha_K\end{bmatrix}\begin{bmatrix}p_K\\ q_K\\ r_K\end{bmatrix} + \left(\frac{1}{m\,V}\right)\\ &\quad\begin{bmatrix}\cos\gamma\cos\mu_K\tan\beta_K & \tan\gamma\sin\mu_K+\tan\beta_K & \tan\gamma\cos\mu_K\cos\beta_K\\ \frac{\cos\gamma\cos\mu_K}{\cos\beta_K} & -\frac{1}{\cos\beta_K} & 0\\ \cos\gamma\sin\mu_K & 0 & \cos\beta_K\cos\gamma\end{bmatrix}\begin{bmatrix}-W\\ L_a\\ Y_a\end{bmatrix}\end{aligned} \tag{10}$$

Equations (9) and (10) express a general kinematic relationship that also stays valid for cases in which the described aerial vehicle operates in windy conditions. Nevertheless, to simplify the notation for this paper, the nonexistence of wind is assumed. In that considered case, the inertial axes denoted by the index K correspond with the aerodynamic axes denoted by the index a. In order to further simplify the used notation, in the rest of the paper, the vectorial quantities, described in the inertial axes denoted by the index K, are used without the corresponding index. This simplification does not noticeably impact the quality of results as the impact of the wind velocity are very small compared to the translation momentum $m\,V$ in the considered case. The mentioned assumptions and simplifications lead to the following simplified notation, in which the K and a indices are dropped:

$$\begin{bmatrix}\mu_K\\ \alpha_K\\ \beta_K\end{bmatrix} = \begin{bmatrix}\mu_a\\ \alpha_a\\ \beta_a\end{bmatrix} = \begin{bmatrix}\mu\\ \alpha\\ \beta\end{bmatrix} \tag{11}$$

$$\begin{bmatrix}\gamma_a\\ \chi_a\end{bmatrix} = \begin{bmatrix}\gamma\\ \chi\end{bmatrix} \tag{12}$$

$$\begin{bmatrix}p_K\\ q_K\\ r_K\end{bmatrix} = \begin{bmatrix}p\\ q\\ r\end{bmatrix} \tag{13}$$

The lift force L_a and the side force Y_a are computed based on the presented high-fidelity non-linear aerodynamic database. The aerodynamic model is formulated as a function of the angle of attack α, sideslip angle β, Mach number Ma, altitude H and the control deflection vector δ. The model provides an independent computation of the control effectiveness and their respective aerodynamic forces and moments. At the current point, the influences of the flaps on the vehicle's dynamics are assumed to be linear, but it is also planned to consider the non-linear effects of the flap deflections in future steps of the research process.

2.4 Open-loop analysis

For the analysis of the modes of the vehicle, the non-linear simulation model is trimmed using a Newton's method-based root-finding algorithm and then linearised at the found trim points. Equations 14 and 15 are showing the linear time-invariant (LTI) state-space system, which is commonly used to describe linear flight dynamics:

$$\dot{x} = A\,x(t) + B\,u(t) \tag{14}$$

$$y = C\,x(t) + D\,u(t) \tag{15}$$

The researchers in Ref. [28] and Ref. [29] observed that specific hypersonic waverider configurations, including the presented vehicle, tend to have unstable open-loop behaviour in the longitudinal and lateral-directional motion characteristics. The obtained results from the eigenmode analysis for the GHGV-2 confirm those findings and it can be seen that the open-loop system is longitudinally statically unstable and laterally dynamically unstable (Dutch roll). A stability-augmentation system (SAS) is needed to artificially stabilise both the longitudinal and lateral dynamics (Figs. 6, 7).

3 Non-linear dynamic inversion and model following control

The main principle of NDI is to linearise the input–output relationship of a non-linear input-affine system by using state feedback and coordinate transformation rather than Jacobian linearisation [30]. Consequently, the dynamics of the controlled variables are reduced to simple integrator dynamics. As a result, the system can be controlled using linear control methods [31]. In order to prevent inversion errors, the method requires a well-known open-loop model of the controlled system's dynamics. However, a robust linear controller design has shown to be capable of dealing with these modeling errors. For further discussions, we consider the following non-linear control affine system of the following form:

$$\dot{x} = f(x) + g(x)u \tag{16}$$

$$y = h(x) \tag{17}$$

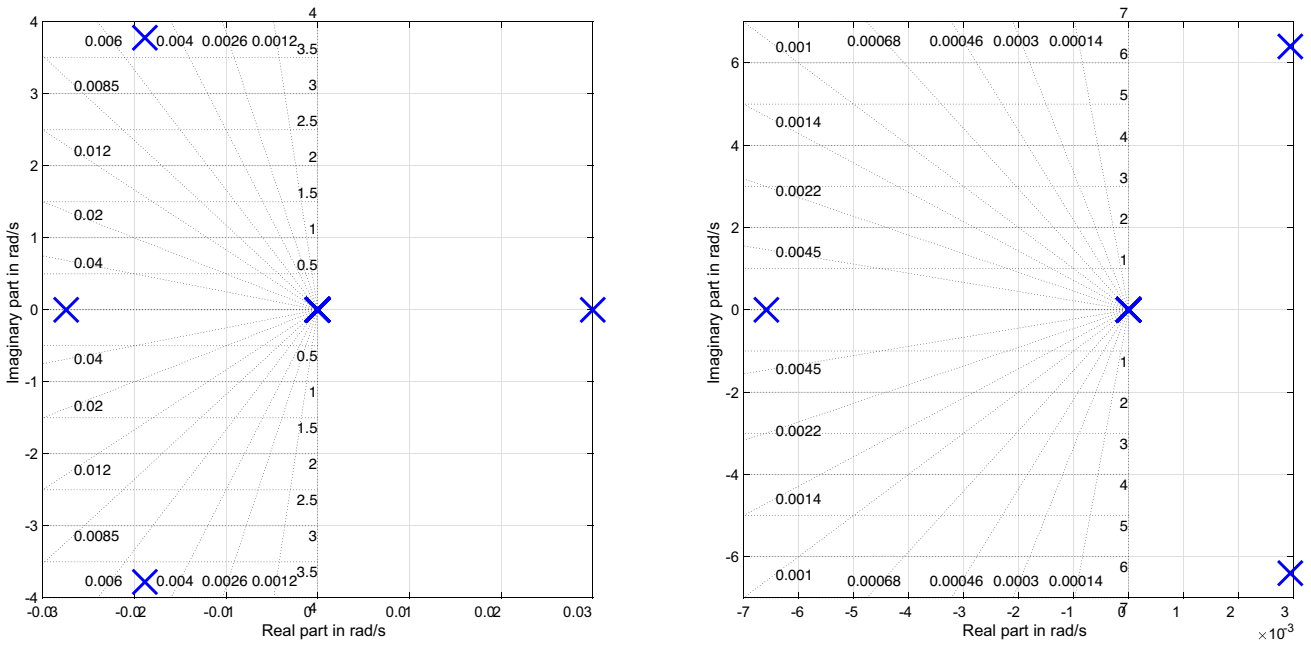

(a) Longitudinal poles (b) Lateral-directional poles

Fig. 6 Exemplary results of the eigenvalue analysis of the linearised open-loop dynamics of the GHGV-2 at Mach 12.5 and at a constant altitude within the height band of the mesosphere

The time derivative of the introduced non-linear dynamics are obtained and reformulated using the Lie derivative notation [32]:

$$\begin{aligned} y^{(1)} = \dot{y} &= \frac{\partial y}{\partial t} = \left(\frac{\partial h}{\partial x}\right)^T \dot{x} \\ &= \left(\frac{\partial h}{\partial x}\right)^T \left[f(x) + g(x)u\right] \\ &= \left(\frac{\partial h}{\partial x}\right)^T f(x) + \left(\frac{\partial h}{\partial x}\right)^T g(x)u \\ &= L_f h + L_g h u \end{aligned} \tag{18}$$

A relationship between the input and the output can be established if $L_g h \neq 0$. For the case $L_g h = 0$, the relationship must be further derived until the system input directly affects the system output. The number of time derivations needed is called the relative degree and is represented by r. Based on the methodology, the input–output of a MIMO system can be described as:

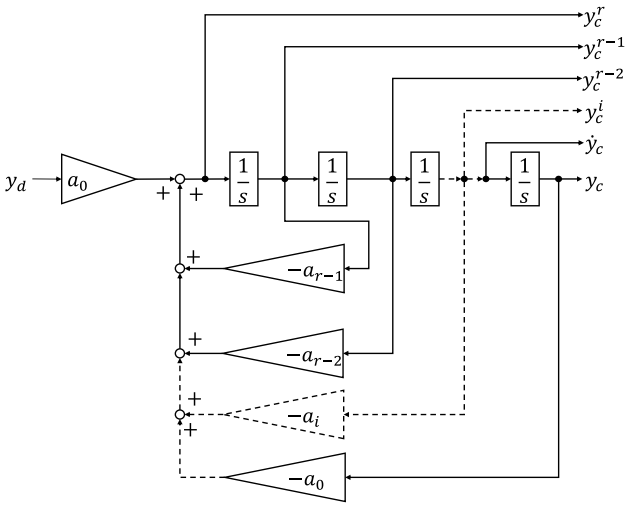

Fig. 7 Sketch of reference model of arbitrary relative degree

$$\begin{pmatrix} y^{(1)} \\ \vdots \\ y^{(r_m)} \end{pmatrix} = \underbrace{\begin{pmatrix} L_f^{r_1} h_1(x) \\ \vdots \\ L_f^{r_m} h_m(x) \end{pmatrix}}_{b(x)} + \underbrace{\begin{bmatrix} L_{g_1} L_f^{r_1-1} h_1(x) & \dots & L_{g_m} L_f^{r_1-1} h_1(x) \\ \vdots & \ddots & \vdots \\ L_{g_1} L_f^{r_m-1} h_m(x) & \dots & L_{g_m} L_f^{r_m-1} h_m(x) \end{bmatrix}}_{A(x)} \underbrace{\begin{pmatrix} u_1 \\ \vdots \\ u_m \end{pmatrix}}_{u} \tag{19}$$

with $A(x)$ being an $m \times m$ non-singular decoupling matrix and $b(x)$ being a $m \times 1$ vector reflecting the non-control effector-related dynamics of the system. For a shorter notation, the inferred relationship is further described as follows:

$$\begin{pmatrix} y^{(1)} \\ \vdots \\ y^{(r_m)} \end{pmatrix} = b(x) + A(x)u \tag{20}$$

In the context of model reference following control, the controlled variables should follow a desired reference trajectory. The reference model for an r^{th} order system is defined in the following form:

$$\begin{pmatrix} y_c^{(1)} \\ \vdots \\ y_c^{(r_m)} \end{pmatrix} = \begin{bmatrix} 0 & 1 & \dots & 0 \\ \vdots & \vdots & \ddots & \vdots \\ -a_0 & -a_1 & \dots & a_{r-1} \end{bmatrix} \begin{pmatrix} y_c \\ \vdots \\ y_c^{(r_m-1)} \end{pmatrix} + \begin{pmatrix} 0 \\ \vdots \\ a_0 \end{pmatrix} y_d \tag{21}$$

with a_i being chosen to impose the desired reference response.

Due to the feedback linearisation, the error dynamics between the reference signal and the vehicle response can be controlled using a linear controller of the following form:

$$\begin{pmatrix} \Delta y^{(1)} \\ \vdots \\ \Delta y^{(r_m)} \end{pmatrix} = -K \left(\begin{pmatrix} y_c \\ \vdots \\ y_c^{(r_m-1)} \end{pmatrix} - \begin{pmatrix} \hat{y} \\ \vdots \\ \hat{y}^{(r_m-1)} \end{pmatrix} \right) \tag{22}$$

with $\hat{y}^{r-i}$ being the measured states and K being a Hurwitz gain matrix. Combined with the derived system output equation, we obtain the required control input:

$$u = A^{-1}(x) \left(\begin{pmatrix} \dot{y}_c \\ \vdots \\ y_c^{(r_m)} \end{pmatrix} - K \left(\begin{pmatrix} y_c \\ \vdots \\ y_c^{(r_m-1)} \end{pmatrix} - \begin{pmatrix} \hat{y} \\ \vdots \\ \hat{y}^{(r_m-1)} \end{pmatrix} \right) - b(x) \right) \tag{23}$$

It should be noted that a cascaded variant of the presented approach is also possible. In this case, an outer loop can generate the reference variables for an inner loop. An explicit multiple-time derivation of the initial equation can thus be avoided and substituted by a clever linkage of known relationships. However, the relative degree of the overall system remains unaffected by this approach. Both cascaded and non-cascaded approaches are used for the application in the flight control system presented in the next section.

4 Integrated non-linear model following control design

For the GHGV-2, a non-linear model-following control system was designed and integrated. The overall structure of the established controller is displayed in Fig. 8. The architecture uses a second-order reference model (RM) system to filter the command input vector $(\mu_d, \alpha_d, \beta_d)^T$ and to shape the desired reference signal vector $(\mu_r, \alpha_r, \beta_r)^T$. The generated reference signals are the filtered commands and the corresponding first and second derivatives of the desired model response. The RM can comprise further knowledge of physical limitations of the system and prevents the controllers from generating unworkable commands. Such limitations can originate from structural and thermal load limits that the vehicle should not exceed. Other influences that can be regarded within the RM limitations are that the actuator capabilities of vehicles operating in high-speed regimes can significantly vary over the flight envelope due to external factors, such as high dynamical pressure and thermal influences acting on the fins. Such influences can limit the vehicle's actuation capacity and restrict the maximum achievable accelerations the control surfaces can provide.

The controller needs to perform two main control tasks: tracking and regulation. The first task is taken over by a model-based feedforward control approach which transforms the computed higher-order derivatives of the reference signals based on known systems kinematics and dynamics. The second task is taken over by a cascaded non-linear dynamic inversion control system which handles uncertainties and reject external disturbances.

The cascaded controller corresponds to a so-called two-loop controller architecture with distinct cascaded outer (attitude control) and inner (body-rates control) loop controllers.

Such a control architecture is particularly easy to tune when a certain amount of time-scale separation can be assumed between the loops (typically factor 5 between the respective bandwidths of these loops), but also also applicable even without it. In that case, the tuning of the controllers will usually influence each other and therefore they need to be tuned, or at least evaluated, together. The bandwidth of the inner loop can in principle be increased by using a fairly aggressive (high-gain) inner loop controller. This is quite often done for missiles and would be undesirable for large aeroplanes (often due to structural loads). Whether such tuning is acceptable or even desirable for a vehicle like the GHGV-2 remains unclear at the

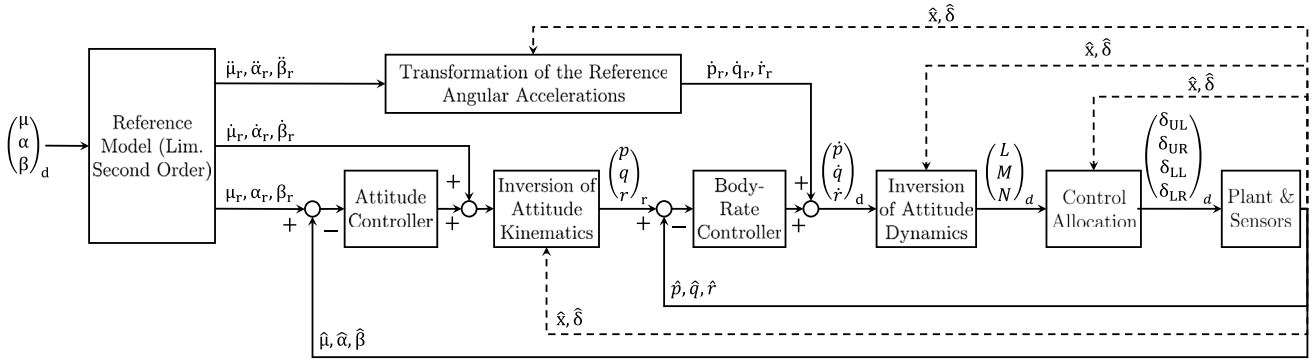

Fig. 8 Overview of the proposed non-linear model following control architecture for the GHGV-2

present stage of this work. Apart from adverse effects with potential coupling with flexible modes, the robustness to delays in the control loop and to unmodelled dynamics may also become problematic with such high-gain inner loop controllers.

4.1 Non-linear cascaded feedback control design

The integrated cascaded feedback control approach is based on the idea of timescale-separated non-linear dynamic inversion systems presented in [5, 6], but is adapted to match the technical realisation of the controlled generic hypersonic glide vehicle.

The input of the linear outer loop controllers is the time-dependent tracking error vector $(e_\mu, e_\alpha, e_\beta)^T = ((\mu_r - \hat{\mu}), (\alpha_r - \hat{\alpha}), (\beta_r - \hat{\beta}))^T$, which is computed based on the state measurements and the obtained tracking commands of the RM (as explained in Sect. 4.3). The implemented linear controllers regulate the system's error dynamics by computing the derivatives of the aerodynamic angles needed to eliminate the attitude control error:

$$\begin{aligned}\begin{bmatrix}\Delta\dot{\mu}\\ \Delta\dot{\alpha}\\ \Delta\dot{\beta}\end{bmatrix} &= K_{P,\mu\,\alpha\,\beta}\begin{bmatrix}e_\mu\\ e_\alpha\\ e_\beta\end{bmatrix} + K_{I,\mu\,\alpha\,\beta}\begin{bmatrix}\int e_\mu\\ \int e_\alpha\\ \int e_\beta\end{bmatrix}\\ &= \begin{bmatrix}K_{P,\mu} & 0 & 0\\ 0 & K_{P,\alpha} & 0\\ 0 & 0 & K_{P,\beta}\end{bmatrix}\begin{bmatrix}e_\mu\\ e_\alpha\\ e_\beta\end{bmatrix}\\ &\quad + \begin{bmatrix}K_{I,\mu} & 0 & 0\\ 0 & K_{I,\alpha} & 0\\ 0 & 0 & K_{I,\beta}\end{bmatrix}\begin{bmatrix}\int e_\mu\\ \int e_\alpha\\ \int e_\beta\end{bmatrix}\end{aligned} \tag{24}$$

The required first-order time derivatives of the aerodynamic angles are obtained by combining the reference model output vector $(\dot{\mu}_r, \dot{\alpha}_r, \dot{\beta}_r)^T$ and the generated feedback control signal vector $(\Delta\dot{\mu}, \Delta\dot{\alpha}, \Delta\dot{\beta})^T$.

$$\begin{bmatrix}\dot{\mu}_{req}\\ \dot{\alpha}_{req}\\ \dot{\beta}_{req}\end{bmatrix} = \begin{bmatrix}\dot{\mu}_r\\ \dot{\alpha}_r\\ \dot{\beta}_r\end{bmatrix} + \begin{bmatrix}\Delta\dot{\mu}\\ \Delta\dot{\alpha}\\ \Delta\dot{\beta}\end{bmatrix} \tag{25}$$

The command input for the inner loop controllers can be computed by inverting the angular kinematics relationships from Eq. (10):

$$\begin{bmatrix}p_r\\ q_r\\ r_r\end{bmatrix} = T_1^{-1}\left(\begin{bmatrix}\dot{\mu}_{req}\\ \dot{\alpha}_{req}\\ \dot{\beta}_{req}\end{bmatrix} - \left(\frac{1}{mV}\right)T_3\begin{bmatrix}-W\\ L_a\\ Y_a\end{bmatrix}\right) \tag{26}$$

The input of the linear inner loop controller is the time-dependent tracking error vector $[e_p, e_q, e_r]^T = \left[(p_r - \hat{p}), (q_r - \hat{q}), (r_r - \hat{r})\right]^T$, which is computed based on the state measurements and the obtained commands of the angular dynamic inversion step described in Eq. (26). The implemented linear controllers regulate the system's error dynamics by computing the angular acceleration commands needed to eliminate the rate control error:

$$\begin{aligned}\begin{bmatrix}\Delta\dot{p}\\ \Delta\dot{q}\\ \Delta\dot{r}\end{bmatrix} &= K_{P,p\,q\,r}\begin{bmatrix}e_p\\ e_q\\ e_r\end{bmatrix} + K_{I,p\,q\,r}\begin{bmatrix}\int e_p\\ \int e_q\\ \int e_r\end{bmatrix}\\ &= \begin{bmatrix}K_{P,p} & 0 & 0\\ 0 & K_{P,q} & 0\\ 0 & 0 & K_{P,r}\end{bmatrix}\begin{bmatrix}e_p\\ e_q\\ e_r\end{bmatrix}\\ &\quad + \begin{bmatrix}K_{I,p} & 0 & 0\\ 0 & K_{I,q} & 0\\ 0 & 0 & K_{I,r}\end{bmatrix}\begin{bmatrix}\int e_p\\ \int e_q\\ \int e_r\end{bmatrix}\end{aligned} \tag{27}$$

The total desired rotational acceleration vector $[\dot{p}_d, \dot{q}_d, \dot{r}_d]^T$ is then obtained by adding the command from the feedback controller $([\Delta\dot{p}, \Delta\dot{q}, \Delta\dot{r}]^T)$ to the feedforward command $[\dot{p}_r, \dot{q}_r, \dot{r}_r]^T$ from the command filter (cf. Sect. 4.2 for further details).

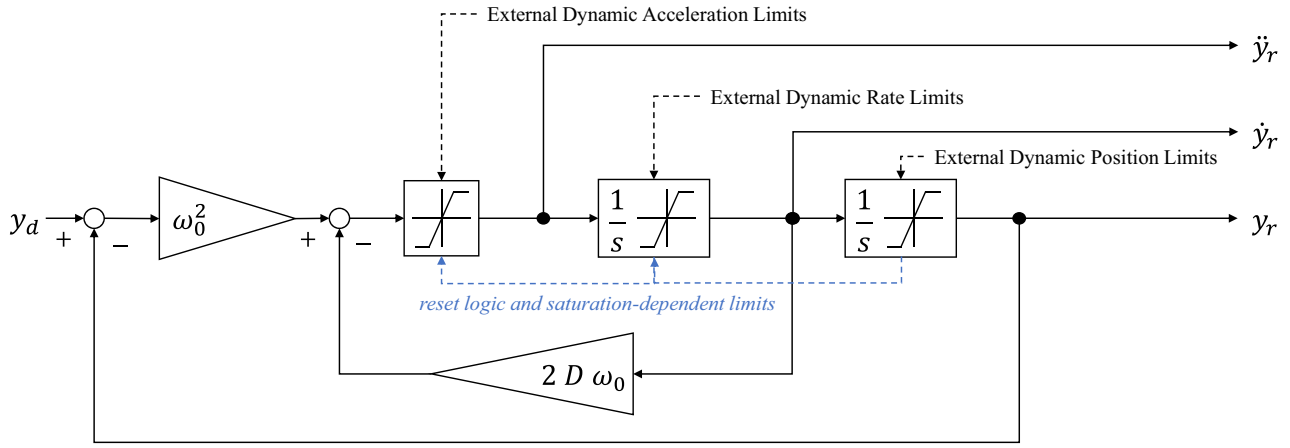

Fig. 9 Exemplary illustration of the simplified-second order reference model used in the different control channels of the integrated NMFC system

$$\begin{bmatrix}\dot{p}_d\\ \dot{q}_d\\ \dot{r}_d\end{bmatrix} = \begin{bmatrix}\dot{p}_r\\ \dot{q}_r\\ \dot{r}_r\end{bmatrix} + \begin{bmatrix}\Delta\dot{p}\\ \Delta\dot{q}\\ \Delta\dot{r}\end{bmatrix} \tag{28}$$

This commanded rotational acceleration vector is then converted to the desired moment vector $\vec{Q}_d$ by considering the vehicle inertia matrix I and the balance of angular momentum (i.e. the gyroscopic moment that the vehicle, in its current state, will be subject to):

$$\vec{Q}_d = \begin{bmatrix}L_d\\ M_d\\ N_d\end{bmatrix} = I\begin{bmatrix}\dot{p}_d\\ \dot{q}_d\\ \dot{r}_d\end{bmatrix} + \begin{bmatrix}\hat{p}\\ \hat{q}\\ \hat{r}\end{bmatrix} \times I \begin{bmatrix}\hat{p}\\ \hat{q}\\ \hat{r}\end{bmatrix} \tag{29}$$

4.2 Non-linear feedforward control design

The integrated non-cascaded, non-linear dynamic inversion-based feedfoward approach uses a generalised reference model and knowledge of the system dynamics. Figure 9 illustrates a simplified version of the second-order RM which is applied to filter the command inputs and shape the desired reference signals. By using a priori known dynamic limits of the vehicle, this reference model ensures that the reference signals sent to the attitude control loop can be achieved, reducing the need for further protections, at least in the nominal/failure-free case.

When none of these limits is reached, the incoming commands from the guidance system $(\mu_d, \alpha_d, \beta_d)^T$ are shaped by second-order transfer functions which can be described in the following form:

$$G_r(s) = \frac{\omega_0^2}{s^2 + 2\,D\,\omega_0\,s + \omega_0^2} \tag{30}$$

The eigenfrequency ω_0 and the damping ratio D of the transfer functions can be chosen such that the desired system response behaviour can be imposed on the vehicle. Besides the desired angular state reference signals, the reference models also generate the first- and second-order derivatives of the desired response. These signals feedforward control information to the inner and outer loop controllers, increasing the system's tracking performance. Figure 10 shows all signals generated by the RM and how the proposed NMFC control system uses them.

The additional usage of the the first- and second-order derivatives of the desired response enables partial decomposition of the command tracking tasks from the regulation tasks of the feedback control system and hence eases up the tuning and decreases the possibility of high-gain solutions. As described in Fig. 10, the first-order time derivative vector of the shaped reference responses $(\dot{\mu}_r, \dot{\alpha}_r, \dot{\beta}_r)^T$ are fed forward to the inner loop inversion of the attitude kinematics. The second-order time derivatives of the shaped reference responses $(\ddot{\mu}_r, \ddot{\alpha}_r, \ddot{\beta}_r)^T$ are used for feedforward purposes by using the known kinematic relationship presented in Eq. (9). Following the NDI methodology discussed earlier, the regarded dynamic relationship needs to be further derived to obtain the final input–output connection that matches the second-order derivatives of the aerodynamic angular signals [27]:

$$\begin{bmatrix}\dot{p}_r\\ \dot{q}_r\\ \dot{r}_r\end{bmatrix} = T_1^{-1}\left[\begin{pmatrix}\ddot{\mu}_r\\ \ddot{\alpha}_r\\ \ddot{\beta}_r\end{pmatrix} - \dot{T}_1\begin{pmatrix}\hat{p}\\ \hat{q}\\ \hat{r}\end{pmatrix} - \dot{T}_2\begin{pmatrix}\dot{\hat{\gamma}}\\ \dot{\hat{\chi}}\end{pmatrix} - T_2\begin{pmatrix}\ddot{\hat{\gamma}}\\ \ddot{\hat{\chi}}\end{pmatrix}\right] \tag{31}$$

Leading to the angular acceleration command vector $(\dot{p}_r, \dot{q}_r, \dot{r}_r)^T$, which is used as a feedforward angular acceleration command signal and later merged with the angular acceleration command vector from the cascaded feedback controller as shown in Eq. (28).

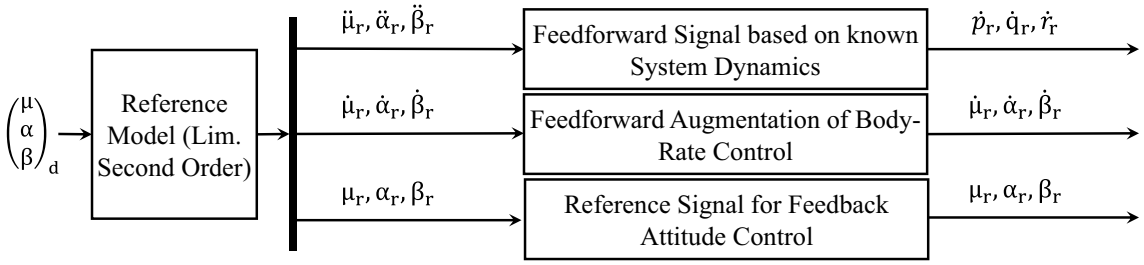

Fig. 10 Conceptual illustration of the generated signals of the reference model and their use in the NMFC

4.3 Linear control allocation design for the endoatmospheric flight phase

As described in Section 2.1, the application of suitable control allocation algorithms for the over-actuated GHGV-2 is required in the exoatmospheric and endoatmospheric flight regimes. However, due to the brevity of this paper, only the control allocation problem for the endoatmospheric flight phase is further discussed. Figure 11 shows the available control surfaces with the connected deflections of the upper left fin δ_{UL}, upper right fin δ_{UR}, lower left fin δ_{LL} and lower right fin δ_{LR} for the described case.

The aerodynamic coefficient derivatives with the control surface deflections can be fairly well approximated by linear terms and so let B be the following control effectiveness matrix:

$$B = \begin{bmatrix} \frac{\partial L}{\partial \delta_{UL}} & \frac{\partial L}{\partial \delta_{UR}} & \frac{\partial L}{\partial \delta_{LL}} & \frac{\partial L}{\partial \delta_{LR}} \\ \frac{\partial M}{\partial \delta_{UL}} & \frac{\partial M}{\partial \delta_{UR}} & \frac{\partial M}{\partial \delta_{LL}} & \frac{\partial M}{\partial \delta_{LR}} \\ \frac{\partial N}{\partial \delta_{UL}} & \frac{\partial N}{\partial \delta_{UR}} & \frac{\partial N}{\partial \delta_{LL}} & \frac{\partial N}{\partial \delta_{LR}} \end{bmatrix}. \tag{32}$$

B is of size 3×4 and thus cannot be inverted. The control effectiveness matrix B depends on the current flight point and states. In order to cope with that dependencies during the mission, the B matrix is continuously re-computed by using an onboard plant model and sensor measurements but it is assumed to be constant for each time step.

For determining the needed control surface deflection $\vec{\delta}_d$ for the actuators, a suitable solution to the following equation needs to be found:

$$\vec{Q}_d = B\,\vec{\delta} \quad \text{with } \vec{\delta} = \begin{bmatrix} \delta_{UL} \\ \delta_{UR} \\ \delta_{LL} \\ \delta_{LR} \end{bmatrix} \tag{33}$$

Equation (33) is an under-determined linear system of equations with 3 equations and 4 unknowns. In general, and here in particular when neglecting further constraints like deflection limits and rate limits, such under-determined problems have an infinite number of solutions. Often some preferences

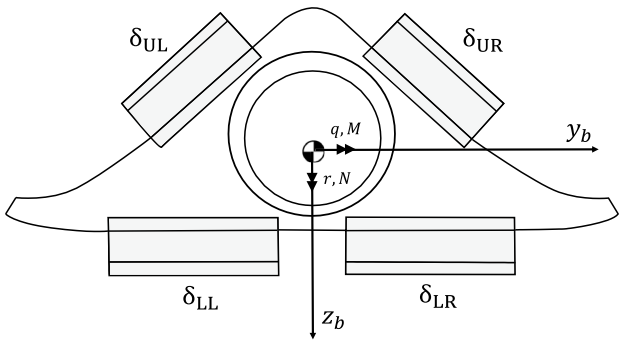

Fig. 11 A conceptual sketch with a rear view on the GHGV-2 and the available control effectors during endoatmospheric operations

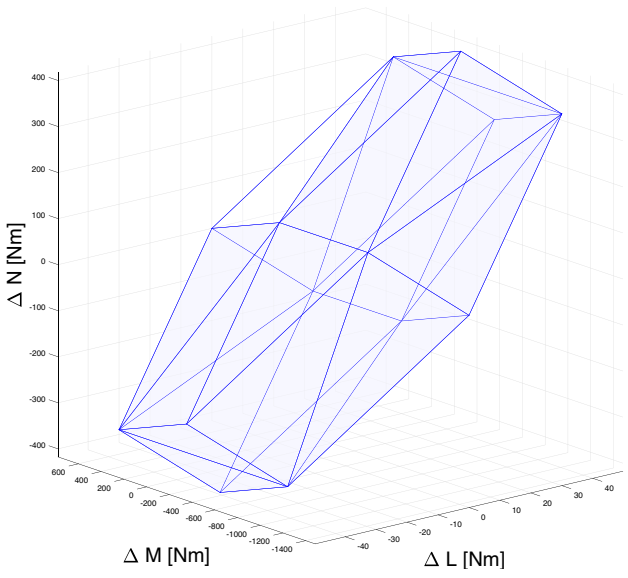

Fig. 12 Exemplary representation of the attainable moment set (AMS) for GHGV-2 for an operating point at $Ma = 8$ and $H = 30$ km

exist, among the infinite number of solutions, and the problem can be schematically formulated as:

$$\begin{aligned} &\underset{\vec{\delta}\in\mathbb{R}^{n_u}}{\arg\min} \quad J(\vec{\delta}) \\ &\text{subject to } \vec{Q}_d = B\,\vec{\delta} \end{aligned} \tag{34}$$

with the cost function J used to express the preference of the control designer and n_u the number of control effectors available. In the most common case, the solution minimising the l_2-norm (also often referred to as min-norm) of $\vec{\delta}_d$ is preferred. For this case, a closed-form solution can be easily obtained via the Moore-Penrose pseudoinverse B^+ of B:

$$\vec{\delta}_c = B^+ \vec{Q}_d = B^T \left(BB^T\right)^{-1} \vec{Q}_d \tag{35}$$

The closed-form solution of Eq. (35) does not consider constraints on the solution of $\vec{\delta}_d$, such as as the deflection limits $\vec{\delta}_{min/max}$ and rate limits $\dot{\vec{\delta}}_{min/max}$ of the actuators. Iterative solutions to the described constrained linear control allocation scheme based on a pseudoinverse exist and are able to consider magnitude and rate limits, see for instance [12, 33–35]. In general, the control allocation problem need to be regarded as a constraint optimisation problem since magnitude and rate limitations on each control effector δ_i are present. The limitations are often defined as individual lower and upper bounds, leading to the following formulation of the feasible set of control inputs Δ:

$$\boldsymbol{\Delta} := \{\delta \in \mathbb{R}^{n_u} \quad | \quad \forall i \in [1, n_u] : \delta_{min,i} \leq \delta_i \leq \delta_{max,i}\} \tag{36}$$

The magnitude limits for each effector are represented using the following saturation function $R_{\delta_i}(\delta_i(t))$:

$$\begin{aligned} &\forall (i,t) \in [1, n_u] \times \mathbb{R},\ R_{\delta_i}(\,\delta_i(t)\,) \\ &\quad = \min\big(\,\delta_{max,i}\,,\, \max\big(\,\delta_{min,i}\,,\,\delta_i(t)\,\big)\,\big) \end{aligned} \tag{37}$$

Based on the feasible set of control inputs, a feasible physical control volume D can be constructed as:

$$D := \{\vec{Q} \in \mathbb{R}^o \quad | \quad \vec{Q} = B\,\vec{\delta} \quad \text{and} \quad \vec{\delta} \in \boldsymbol{\Delta}\}\,. \tag{38}$$

In the context of flight control, the resulting convex set D is often referred to as the attainable moment set (AMS) [36]. An example of an AMS for a hypersonic glide vehicle with four control effectors ($n_u = 4$) is shown in Fig. 12.

The resulting control allocation problem of the GHGV-2 can be formulated as the following constrained optimisation problem:

$$\begin{aligned} &\underset{\vec{\delta}\in\mathbb{R}^{n_u}}{\arg\min} \quad \|\vec{\delta}\|_p \\ &\text{subject to } \vec{Q}_d = B\,\vec{\delta} \\ &\qquad\qquad \vec{\delta}_{min} \leq \vec{\delta} \leq \vec{\delta}_{max} \\ &\qquad\qquad \dot{\vec{\delta}}_{min} \leq \dot{\vec{\delta}} \leq \dot{\vec{\delta}}_{max} \end{aligned} \tag{39}$$

with p being a real number used to define the considered norm. In this work and without further discussion, the l_2-norm was chosen. Approaches based on the l_1-norm or the l_∞-norm could also lead to desirable results; interested readers are referred to [37–41] for deeper discussions on the topic of the influences of different norms on the control allocation performance. Based on the decision to minimise the l_2-norm of the least-square problem, the optimisation problem can be be formulated as a quadratic programming control allocation (QPCA) problem. Examples of that can be found in the work presented in Ref. [42] and Ref. [43].

Regardless of the chosen norm, the allocation problem of Eq. (39) could be infeasible. This would happen when the commanded moment vector $\vec{Q}_c$ is not within the AMS. In such case, the following relaxed version can be used instead:

$$\begin{aligned} &\underset{\vec{\delta}\in\mathbb{R}^{n_u}}{\arg\min} \quad \left\|\vec{\delta}\right\|_p + k \left\| W \left(\vec{Q}_d - B\,\vec{\delta}\right)\right\|_p \\ &\text{subject to } \vec{\delta}_{min} \leq \vec{\delta} \leq \vec{\delta}_{max} \\ &\qquad\qquad \dot{\vec{\delta}}_{min} \leq \dot{\vec{\delta}} \leq \dot{\vec{\delta}}_{max} \end{aligned} \tag{40}$$

with k large enough to put sufficient emphasis on the satisfaction of the commanded moment vector $\vec{Q}_d$ and W being a weighting matrix allowing the designer to set priorities between the three commanded moments (pitching, rolling, and yawing) or combinations of these (W can be chosen non-diagonal). The problem of Eq. (40) is always feasible, but may deviate from a near perfect allocation: either if k is chosen too low or if the commanded moment vector $\vec{Q}_d$ is not attainable. The latter case corresponds to a physical limitation of the commanded system which cannot be avoided.

When using the l_2-norm (as in this work), the problem of Eq. (40) is usually equivalently rewritten as a inequality-constrained quadratic problem with the form:

$$\begin{aligned} &\underset{x}{\arg\min} \quad \tfrac{1}{2} x^T P x + q^T x \\ &\text{subject to } A\,x \leq b \end{aligned} \tag{41}$$

for which many standard solvers are available. By defining $x := \vec{\delta}$ and performing some manipulations of the cost function (with $p = 2$) and of the constraints of Eq. (40), the matrices P and A and the vectors q and b of the quadratic problem of Eq. (41) can be expressed based on the terms used in Eq. (40), the current control deflection vector $\vec{\delta}_{cur}$ and the time step ΔT:

$$P = \begin{bmatrix} k\,(B^T W^T W B) \\ I_{n_u \times n_u} \end{bmatrix} \tag{42}$$

$$q = \left[k\,(-2\,B^T W^T W \vec{Q}_c)\right] \tag{43}$$

$$A = \begin{bmatrix} +I_{n_u \times n_u} \\ -I_{n_u \times n_u} \\ +I_{n_u \times n_u} \\ -I_{n_u \times n_u} \end{bmatrix} \tag{44}$$

$$b = \begin{bmatrix} +\vec{\delta}_{max} \\ -\vec{\delta}_{min} \\ +\left(\vec{\delta}_{cur} + \Delta T \cdot \dot{\vec{\delta}}_{max}\right) \\ -\left(\vec{\delta}_{cur} + \Delta T \cdot \dot{\vec{\delta}}_{min}\right) \end{bmatrix} \tag{45}$$

with $I_{n_u \times n_u}$ being the identity matrix of size $(n_u \times n_u)$.

With these definitions, the problems of Eqs.(40) and (41) are equivalent. The formulated quadratic programming control allocation (QPCA) problem can be solved using a variety of methods, such as interior-pint, active-set, or simplex. For the solving the defined QPCA problem a general-purpose solver from [44] was used.

4.4 Integral anti-windup design via pseudo-control hedging

In NDI-based control methodologies, it is often assumed that a time-scale separation between the controlled states and the actuator dynamics is present, and hence, the actuators can follow the control input commands instantaneously [45]. In reality, this is not true, but it is in most cases a sufficient and valid assumption. However, in the presence of critical input characteristics where actuator magnitude limits, actuator rate limits, and linear input dynamics are not neglectable, the made assumption could cause severe problems and undesired dynamical effects. Even though the previously presented model reference system from Sect. 4.2 considers the physical limits in the control input domain; unmodelled dynamics and external disturbances could still lead to performance degradation or even instability of the close loop, which could have been prevented by observing the real reaction of the system and adjusting the commands accordingly. To overcome such problems, the authors in Ref. [46] proposed compensating non-linear actuator effects, such as actuator limitations and linear input dynamics, in the reference model signal. The approach is called Pseudo Control Hedging (PCH) and allows to adapt the reference signal in case of unachievable commands [47]. Further, PCH can act as an anti-windup technique for the PI controllers used to compute the control input of the inner and outer loop [48].

The simplified basic principle of PCH is grounded on the idea that for a control affine system with the relative degree of one, in the form of:

$$\dot{x} = f(x) + g(x)\,\delta \tag{46}$$

The NDI-based control law can then be derived as:

$$\delta = g(x)^{-1}(\nu - f(x)) \tag{47}$$

with ν being called the virtual control input representing the desired $\dot{x}$ signal generated by linear controllers of form of $\nu = -Ke$ and e being the tracking error. Due to the unmodelled control effector characteristics, the actual control input δ_{act} is not identical to the commanded control displacement δ_d. Based on the actual control input δ_{act} the actual virtual control input can be estimated via:

$$\hat{\nu} = f(x) + g(x)\,\delta_{act} \tag{48}$$

The difference between the estimated and commanded virtual control input is defined as $\nu_h = \nu - \hat{\nu}$ and is called the hedging signal and can be used as a compensation signal which is fed back to the reference model to scale (or hedge)

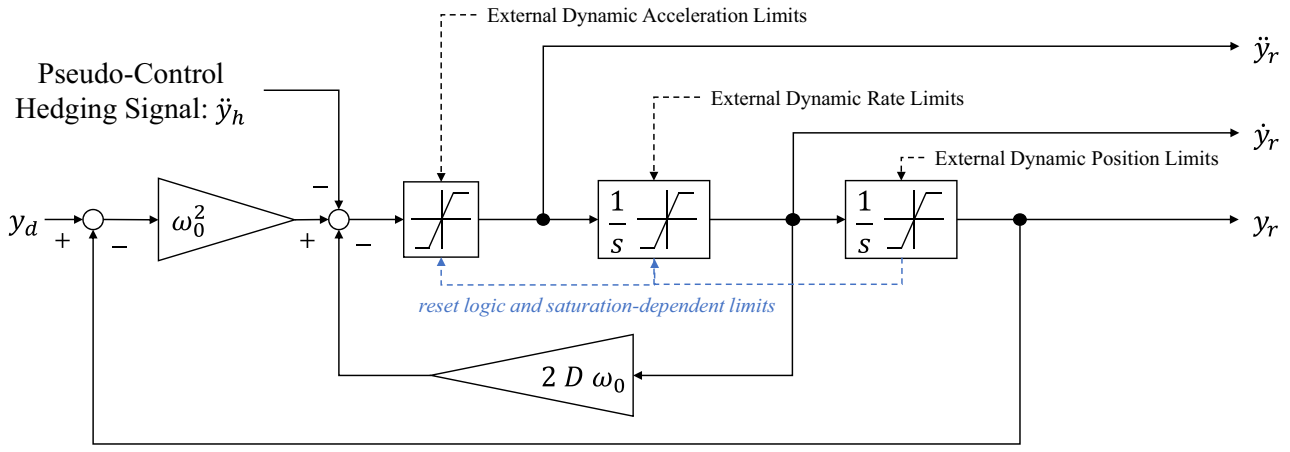

Fig. 13 Exemplary illustration of the simplified-second order reference model used in the different control channels of the integrated NMFC system

Table 1 Information of the regarded trim point for the conducted control performance analysis

Trim point information	
Parameter	Value
Mach number	12.5
Angle of attack α	0°
Angle of sideslip β	0°
Altitude	40 km

the commanded signal down to a level that is achievable for the actuators.

For the here regarded system, we consider (compared to Fig. 9) a slightly modified second-order reference model, shown in Fig. 13. The reference acceleration signal at the output of the RM is computed as:

$$\ddot{y}_r = \omega_0^2 \left(y_c - y_r\right) - 2\,D\,\omega_0\,\dot{y}_r - \ddot{y}_h \tag{49}$$

with ν_h being the hedging signal computed in two steps. In the first step the measured/estimated actuator states are used to compute the acting virtual control input:

$$\begin{bmatrix}\hat{\dot{p}}\\ \hat{\dot{q}}\\ \hat{\dot{r}}\end{bmatrix} = I^{-1}\left(B\,\delta_{act} - \begin{bmatrix}\hat{p}\\ \hat{q}\\ \hat{r}\end{bmatrix} \times I \begin{bmatrix}\hat{p}\\ \hat{q}\\ \hat{r}\end{bmatrix}\right) \tag{50}$$

Afterwards, the difference between the estimated and commanded virtual control input is computed as:

$$\nu_h = \begin{bmatrix}\dot{p}_h\\ \dot{q}_h\\ \dot{r}_h\end{bmatrix} = \begin{bmatrix}\dot{p}_c\\ \dot{q}_c\\ \dot{r}_c\end{bmatrix} - \begin{bmatrix}\hat{\dot{p}}\\ \hat{\dot{q}}\\ \hat{\dot{r}}\end{bmatrix} \tag{51}$$

Since the RM module is not directly computing the angular acceleration in body-fixed frame, the hedging signal ν_h needs to be additionally transformed using Eq. (52) to generate the needed hedging signal vector $(\ddot{\mu}_h, \ddot{\alpha}_h, \ddot{\beta}_h)^T$:

$$\ddot{y}_h = \begin{pmatrix}\ddot{\mu}_h\\ \ddot{\alpha}_h\\ \ddot{\beta}_h\end{pmatrix} = T_1 \begin{bmatrix}\dot{p}_h\\ \dot{q}_h\\ \dot{r}_h\end{bmatrix} + \dot{T}_1 \begin{pmatrix}\hat{p}\\ \hat{q}\\ \hat{r}\end{pmatrix} + \dot{T}_2 \begin{pmatrix}\hat{\dot{\gamma}}\\ \hat{\dot{\chi}}\end{pmatrix} + T_2 \begin{pmatrix}\hat{\ddot{\gamma}}\\ \hat{\ddot{\chi}}\end{pmatrix} \tag{52}$$

The beneficial influence of PCH for this purpose is illustrated in the evaluation results presented in the next section.

5 Simulation results

The proposed NMFC architecture for the GHGV-2 was examined using a non-linear simulation framework. In the subsequent evaluation, the closed-loop control system is evaluated in the following cases:

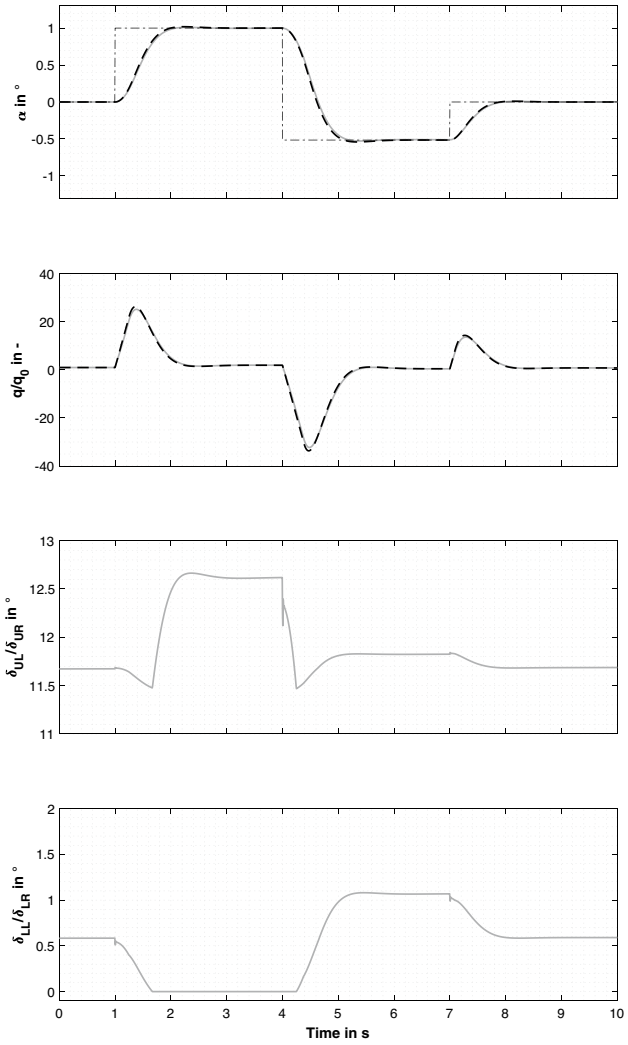

Fig. 14 Simulation results for a doublet command input on α_d in the case with no model uncertainties. Displayed time series: angle of attack α, normalised pitch rate, and fin deflections in %. Dash-dotted black: raw reference command, dashed black: shaped reference signal, grey: vehicle response

- Control performance of the the nominal closed-loop system
- Control performance of the closed-loop system in the presence of control surface damages and control input saturation
- Control performance of the closed-loop system in the presence of static parametric uncertainties of the plant

For the presented empirical evaluation of the NMFC system, a high-fidelity flight dynamics model in a MATLAB/Simulink environment was used. The model was specifically developed for the control design of hypersonic flight vehicles; see [24] for more details. The modelled actuators of the control fins are considered as second-order systems with limits on the magnitude and rate. Within the presented

analysis, the system dynamics of the GHGV-2 have been trimmed around an operating point defined by the parameters listed in Table 1.

5.1 Control performance in the nominal case

Figure 14 presents the evaluation results of the nominal closed-loop system for a simulation case with an angle-of-attack tracking task. In the regarded analysis case, the tracking performance in the pitch channel is evaluated by providing a doublet command on the α_d channel with a magnitude of 1°. The raw doublet reference command on α_d is shown in dash-dotted black, the filtered reference command is shown in dashed black, and the vehicle's response is displayed as a solid grey line.

It can be seen that the proposed controller tracks the given reference signal on the angle-of-attack channel with the desired response characteristics defined in the RM. Since no direct raw pitch rate q is commanded, the shown shaped reference signal of the normalised pitch rate is computed using the $\dot{\alpha}_r$ command of the RM. In order to compare it with a pitch rate in the body-fixed axis, the signal is transformed using the relationship presented in Eq. 26. The vehicle's normalised pitch rate closed-loop response follows the desired pitch rate well and shows beneficial damping characteristics of the inner loop controllers. Since in the regarded pitch manoeuvre, μ and β are set to zero, the manoeuvre is symmetrical. This fact leads to symmetrical deflections on the lower (δ_{LL} and δ_{LR}) and upper flaps (δ_{UL} and δ_{UR}), which can be noticed in the displayed times series. It is of interest for the reader to see how the control allocation methodology, presented in Sect. 4.3, is handling the simple pitch control case. From a flight dynamical point of view, it would be assumed that purely the upper surfaces, δ_{UL} and δ_{UR}, would be needed for a positive α command and the lower surfaces, δ_{LL} and δ_{LR}, for a negative α. Since the flaps on both sides are not able to reach negative deflection angles and hence are limited in the way they contribute to the balance of moment of the vehicle. However, it is interesting to see that in the regarded case for a required positive moment change ΔM, needed to obtain a positive $\Delta\alpha$, the CA at first decreases the deflections of the lower flaps. This makes sense and is also desired from an energy conservation perspective since this behaviour minimises the drag created by control surface deflections. Once the lower flaps have reached the lower magnitude limits, the CA system uses the upper flaps to uphold the desired α_d. The opposite behaviour with a negative $\Delta\alpha$ requirement can as well be observed. This behaviour of the specified CA shows that it is well-conditioned and able to handle the over-actuated system adequately. In a further step, the proposed NMFC was evaluated concerning the lateral-directional control performance. Figure 15 presents the evaluation results for the nominal system model's aerodynamic bank and sideslip angle tracking task. The given analysis case evaluates the tracking performance on the lateral and directional channels by providing two consecutive doublet commands on both μ_d and β_d channels, with μ_d having a maximum magnitude of 40° and β_d having a maximum magnitude of 1°. Again, both raw doublet reference commands on the μ_d and β_d channels are given in dash-dotted black, the filtered reference commands are shown in dashed black, and the vehicle's response is displayed as a solid grey line. It can be seen that the proposed controller is also able to effectively track given μ_d and β_d reference signals in line with the desired response characteristics. It is noticeable that the NMFC structure is, due to the use of kinematic knowledge, able to decouple the lateral-directional dynamics of the system and control both channels separately.

In the regarded lateral-directional manoeuvre, α is kept to the trim value of 0°. Therefore, the default deflections of the surfaces are identical to the trim deflection seen in the prior nominal pitch control case. For the first regarded roll manoeuvre, the CA system is forced to generate a positive ΔL, which is primarily assumed to be obtained by positive deflections of the upper right surface δ_{UR} and the lower left surface δ_{LL} or a decrease of the deflections of the upper left surface δ_{UL} and the lower right surface δ_{LR}. The time series shows that the integrated CA methodology used both options simultaneously. It is also apparent that the system's control surfaces are highly effective around the roll axis and can follow comparably large roll manoeuvres with minimal deflections. This observation can partly be explained by the high dynamic pressure achievable at an operating point with a Mach number of 12.5. However, this changes for the second commanded manoeuvre, in which the controller receives an angle of sideslip command. It is noticeable that the smaller angle of the sideslip command needs much higher surface deflections. This phenomenon of the opposite effect might have two reasons. First, the system is not designed to operate with high angles of sideslip, and hence, the control effectiveness is, by design, significantly lower compared to the control effectiveness around the roll axis. Second, the system has a strong yaw-roll coupling, which has to be compensated. This effect additionally leads to possibly more considerable deflections of all flaps. Nevertheless, for the presented case, it can be stated that the CA system is also well-suited to handle the over-actuated system adequately for roll and sideslip commands.

5.2 Control performance in the presence of control surface damages and control input saturation

This section presents the results obtained within an investigation of the influences of control surface damages and control input saturation on the closed-loop pitch dynamics.

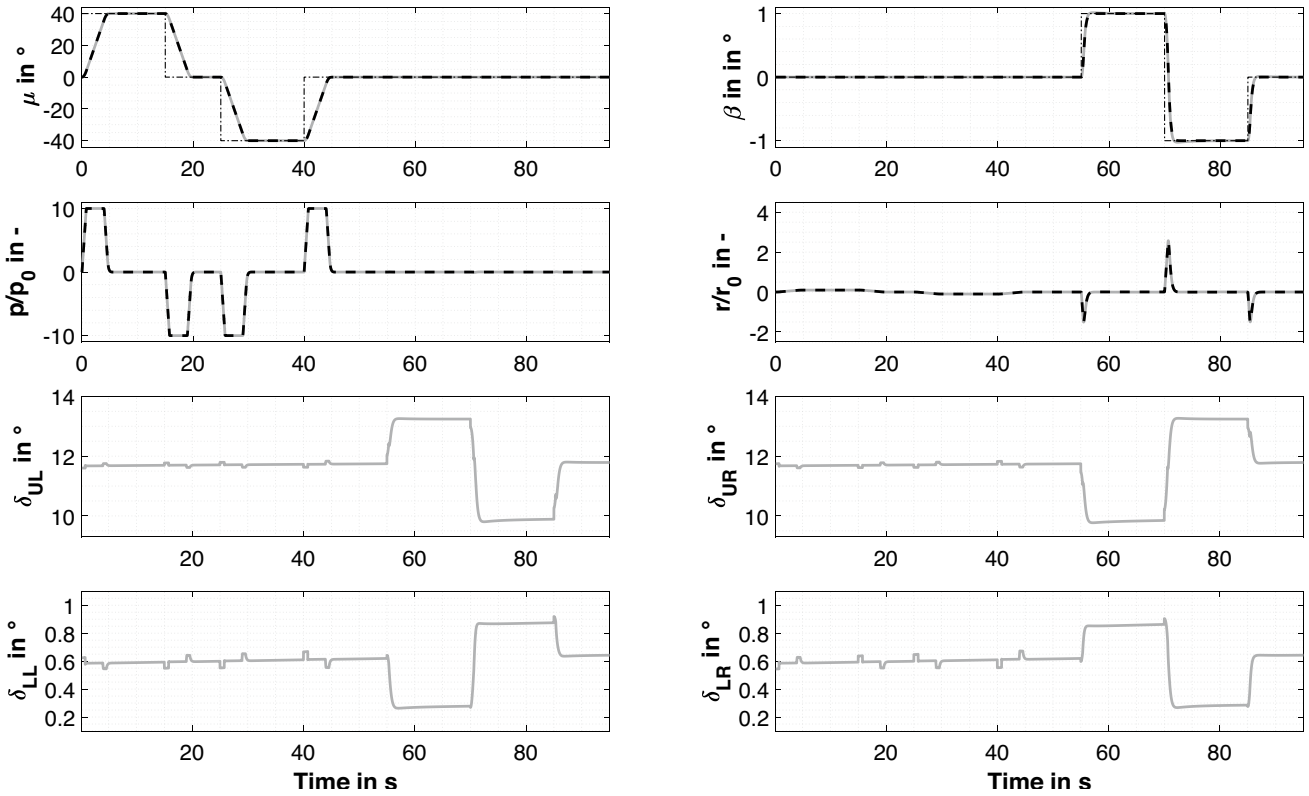

Fig. 15 Simulation results for two consecutive doublet command on the μ_d and β_d in an analysis case with no model uncertainties. Displayed time series: flight path bank angle μ, angle of sideslip β, normalised roll rate, normalised yaw rate and fin deflections in %. Dash-dotted black: raw reference command, dashed black: shaped reference signal, grey: vehicle response

In particular, the examination aims to evaluate the proposed PCH-based anti-windup scheme and its benefits for safe flight operations in the presence of an unknown control effectiveness reduction and limiting magnitude constraints on the actuators. The given analysis case evaluates the tracking performance in the pitch channel by providing two consecutive α_d doublet commands, with each having a magnitude of $\pm 1°$. To assess the effects of control surface damages during a potential operation, the control effectiveness of all control effectors is lowered by 50%. This mimics the potential effects of a surface area loss, which has linear influences for a purely control affine system. The significant lowering of the control surface effectiveness also has the effect that the actuator are forced into saturation for a manoeuvre command in a flight state where saturation normally would not occur. Within the presented analysis, three different control configurations are compared. First, the NMFC, without any implemented anti-windup technique, is used to get a better understanding of the problems related to integrator windup. Second, a modified version of a simple anti-windup technique named "clamping" ensures that the integral controller does not continue to integrate the tracking error once the actuators are saturated [49]. In the most common version of the clamping methodology, the actuator mismatch error between the commanded and the actual actuator state, is directly used to trigger the integrator reset. However, in the here-presented version, the virtual control difference from Eq. (51) is used. The reason for that is that the implemented CA system already considers actuator limits. Hence, it would only propagate feasible commands to the actuators. This would lead to a non-working anti-windup solution since the generally used actuator mismatch error would always be zero, and hence, the integrator would always continue to integrate. Finally, the second considered anti-windup methodology is the PCH approach presented in Sect. 4.4. Figure 16 displays the outcomes of the described examination case. The two raw doublet reference commands on the α_d channel are given in dash-dotted black, the filtered reference commands from the RM are shown in dashed black. The vehicle's response for the system without any anti-windup system is displayed as a solid black line, the system with an implemented clamping scheme is given as a dashed red

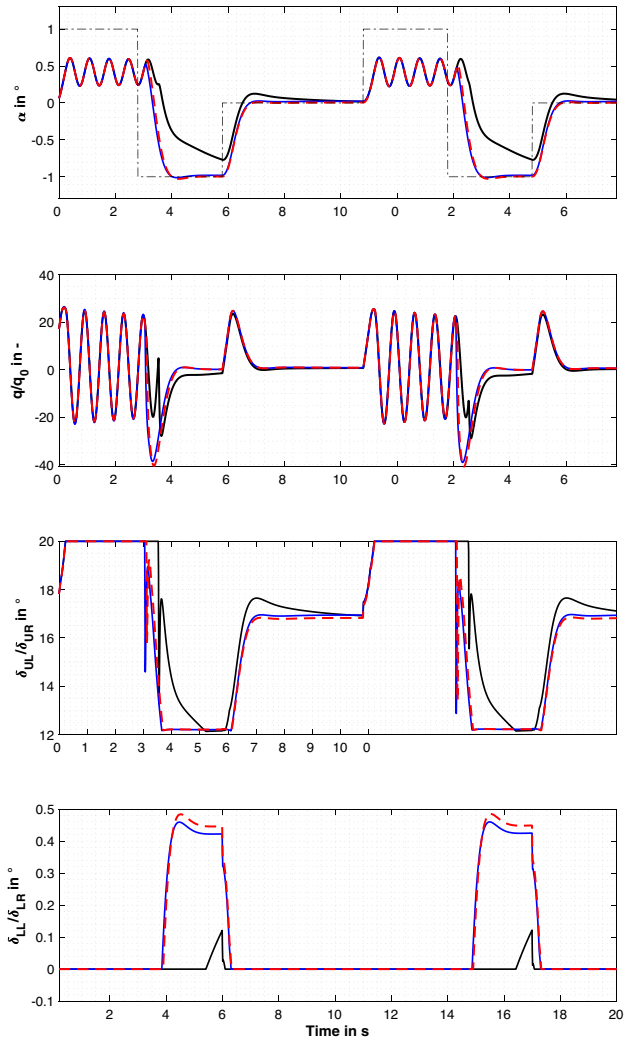

Fig. 16 Simulation results for two consecutive doublet command inputs on α_d in the in the presence of control surface damages and control input saturation. Displayed time series: angle of attack α, normalised pitch rate, and fin deflections in %. Dash-dotted black: raw reference command, solid black: vehicle response for NMFC without anti-windup system, dashed red: vehicle response for NMFC with clamping-based anti-windup approach, solid blue: vehicle response for NMFC with PCH-based anti-windup approach

line, and the NMFC with PCH is shown as a solid blue line. For all regarded closed-loop systems, it can be seen that the vehicle drives into saturation for all actuators after around 0.5 s. The reason for that is that the desired moment command is outside of the AMS and hence the system is not able to generate the needed positive pitch moment change ΔM by either further increasing the upper flap deflections or decreasing the lower flap deflections. Due to the lack of needed Moments the pitch dynamics are under-damped once all relevant actuators are in saturation in the regarded flight state, which explains the visible oscillations. The NFMC, without any anti-windup method, is showing an unacceptable tracking performance. The controller takes comparably long to recover once the saturation state is overcome for the downwards maneuver. It can be assumed that the integrators continue to integrate while the actuators are in saturation. The illustrated problem can be solved by the previously described clamping methodology, in which the integrator is forced to stop integration once the actuators are in saturation. The response of the system with integrator clamping is, at first, similar to the one without any anti-windup mechanism. Nevertheless, the system can recover faster and follow the trajectory once the actuators are no longer saturated. The PCH-based anti-windup approach delivers similar results to the system with clamping by preventing an integrator windup. It is of interest to see that all three systems are able to follow the downwards and the zeroing reference commands properly as long it is physically feasible and no integrator is in windup. This shows that the integrators are capable of handling significant model mismatches between the assumed and the actual control effectiveness of the control inputs. Based on the obtained results, both examined anti-windup methodologies are well suited. However, the PCH also has further benefits, which are projected to support future steps within the ongoing research efforts. It can significantly help minimise undesired effects in the transient phase, e.g., those coming from not modelled or not considered non-linear actuator dynamics, and could further pave the way for future steps towards the use of adaptive control systems in the inner loop [50].

5.3 Control performance in the presence of static parametric uncertainties

In the following analysis case, the robustness of the proposed NMFC is examined against static multiplicative parametric uncertainties. Due to the brevity of this paper, only the control performance on the closed-loop pitch dynamics are looked into. This should not impact the overall validity of the investigations. Further analysis of the authors have shown that a similar robustness assessment for the lateral and directional dynamics would lead to similar conclusions with regards to the overall robustness against parametric uncertainties of the regarded control system. In the presented examination case, the established model was modified such that static parameter deviations for the aerodynamic moment coefficient $C_{m,0}$, aerodynamic z-force coefficient $C_{z,0}$, the distance between the center of pressure and the center of gravity Δx_{cp-cg}, the moment of inertia I_{yy}, and the mass m

Table 2 Chosen uncertainty parameter properties of the conducted robustness analysis of the proposed control architecture

Multiplicative Gaussian uncertainties	
Uncertain parameter	Uncertain spread ($\pm 3\sigma$)
$C_{m,0}$	20 %
$C_{z,0}$	20 %
Δx_{cp-cg}	10 %
m	10 %
I_{yy}	10 %
C_{m,δ_U}	40 %
C_{m,δ_L}	40 %

can be considered. Also, static parameter deviations for the flaps have been looked into. Due to the symmetric nature of the here discussed analysis case, the uncertainties of the upper and lower flaps have been merged regarded as static uncertainty parameter $C_{m,U}$ and $C_{m,L}$. A Gaussian probability density function (PDF) in the form of Eq. 54 was assumed for the uncertainty distribution of the selected parameters.

$$C_{i,j} = \Delta C_{i,j}(\kappa_{i,j}) \cdot C_{i,j,nom} \tag{53}$$

$$\Delta C_{i,j}(\kappa_{i,j}) \sim \mathcal{N}(1, (\kappa_{i,j} \,/\, 3)^2) \tag{54}$$

For each uncertain defined parameter $C_{i,j}$ a maximum uncertainty spreading $\kappa_{i,j}$ around the nominal value $C_{i,j,nom}$ was defined. As Eq. 54 shows, is the considered uncertainty distribution factor $\Delta C_{i,j}$ defined so that the maximum occurring parameter deviation will generally lie within a range of $\pm 3\sigma$ standard deviation around $C_{i,j,nom}$. Regarding the here presented results of the controller's robustness assessment, for each uncertain parameter $C_{i,j}$, a new sample value of the parameter deviation was computed for every simulation run. Table 2 presents the selected uncertain parameters and the defined uncertainty spreadings for the discussed robustness assessment of the proposed controller. A Monte Carlo simulation with a sample size of 1000 simulation runs has been carried out for the analysis. Different to the prior simulation cases, the vehicle was trimmed at an angle-of-attack of $-3°$ and received a mixed reference trajectory leading to the final reference value of $-5°$. Figure 17 presents the acquired results from the analysis case with the considered multiplicative parametric uncertainties. The response of the closed-loop vehicle under the presence of uncertainties is displayed in grey lines, the filtered reference command is shown in a dashed black line, and the response for the system in the nominal case is displayed in a red line. Even though the spread of the responses is quite significant the closed-loop system shows the ability to robustly stabilise the vehicle dynamics and track the given reference signal

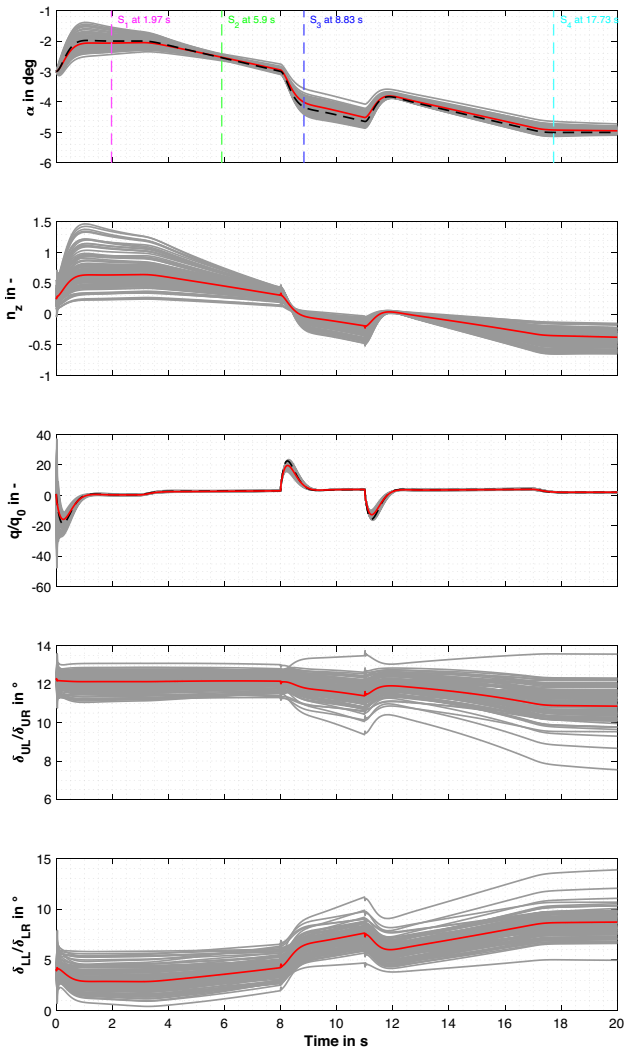

Fig. 17 Simulation results for a command input on α_d in the presence of static model uncertainties. Displayed time series: angle of attack α, load-factor in z-direction, normalised pitch rate, and fin deflections in %. Black dash-dotted: reference command, black rigid: closed-loop vehicle response without integral control, grey: closed-loop vehicle response with integral control

under the presence of the defined model mismatches. This is mainly due to the beneficial properties coming from the used integral controllers. It is assumed by the authors that, due to the integral controllers, the proposed system is able to track any given constant reference signal with a steady-state error as long as the required moments lay within the AMS. For time changing reference signals, a convergence of the vehicle state and the required reference would be more complex and depending on a set on different factors, such as sufficiently high chosen gains of the integral controllers and the slope of change of the commanded reference signal. Figure 17 also indicates how much the load factor n_z is varying in the presence of uncertainties. The nominal value at the time step $T = 1s$ should be at around 0.7, but gets in certain

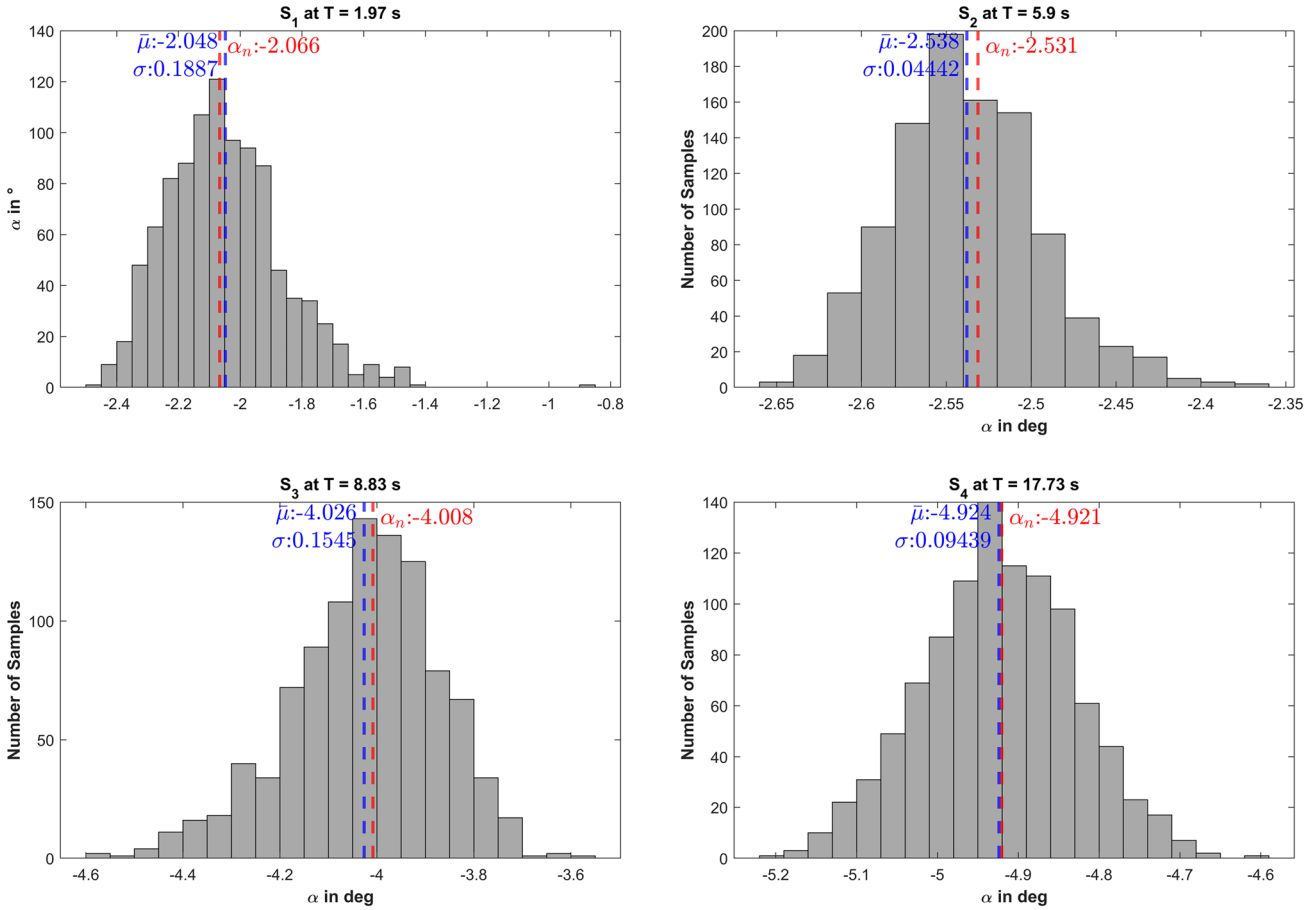

Fig. 18 Histograms of the regarded Monte Carlo analysis for the time sections S_1, S_2, S_3 and S_4

cases up to 4 in the presence of the defined uncertainties. This might could have serious implication on the mission, since the higher load factors in the z-direction could lead to major inaccuracies with regards to intended translational maneuvers. The authors are currently investigating the implication of model uncertainties on the overall mission and plan to share findings in future work. To better understand the presented results of the Monte Carlo analysis, the set of obtained α times series was deeper analysed at four different time sections: S_1 at $T = 1.97$,S_2 at $T = 5.9$,S_3 at $T = 8.83$, and S_4 at $T = 17.73$. The results can be seen in Fig. 18, with the mean value of the distribution being defined as $\bar{\mu}$ and the nominal response value for each time section being defined as α_n. Even though only Gaussian PDFs have been assumed for each parameter, the responses of the uncertain plant show for each time section a different PDF. Implying that for different time steps in the overall manoeuvre, different parameter uncertainties are dominant in the overall dynamics. It is also of interest for readers to see the tendency of convergence between the mean value of the distribution and the response of the nominal system. In the transient phase, towards a changed reference value, both values differ due to the dominance of the model mismatches. However, the integral controllers can bring both together if sufficient time is given. This can be seen in the last regarded time section at $T = 17.73$. To better understand the shifts in the distributions, the influences of the uncertainties at the different time sections have been analysed. In Figs. 19 and 20, the squared error E^2_Δ between the nominal angle of attack response α_n and the uncertain angle of attack responses of the plant for each sample are plotted over the defined uncertainties at each sample. Additionally, for each parameter, the linear fit is given as a red line to get a qualitative understanding of the influences of the uncertainties on the squared error E^2_Δ. Since different manoeuvres are regarded in each time section, it is only possible to look into each time section separately and compare the influences of the parameters relative to each other. Figure 19 indicates that the uncertainties on the parameters $C_{m,0}$, $C_{z,0}$, Δx_{cp-cg} and C_{m,δ_L} have bigger influences on E^2_Δ than the others, due to their steeper slopes of the linear fit. It is physically self-evident that the uncertainties on $C_{m,0}$ influence E^2_Δ. Also, the influences of the other parameters can be explained based on flight physics. This can be compared with Fig. 18. There, the biggest spreads in

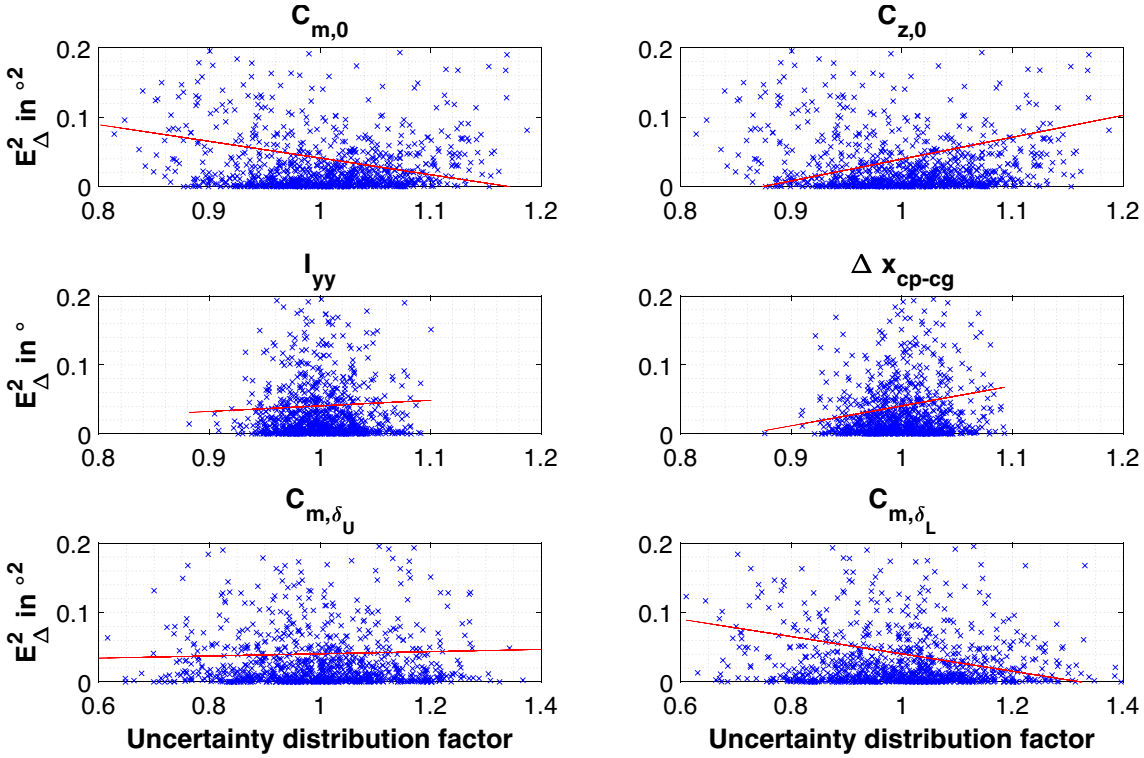

Fig. 19 Simulation results for E_Δ^2 each simulation sample plotted over the uncertainty spreading of each defined uncertain parameter at S_1 at $T = 1.97$

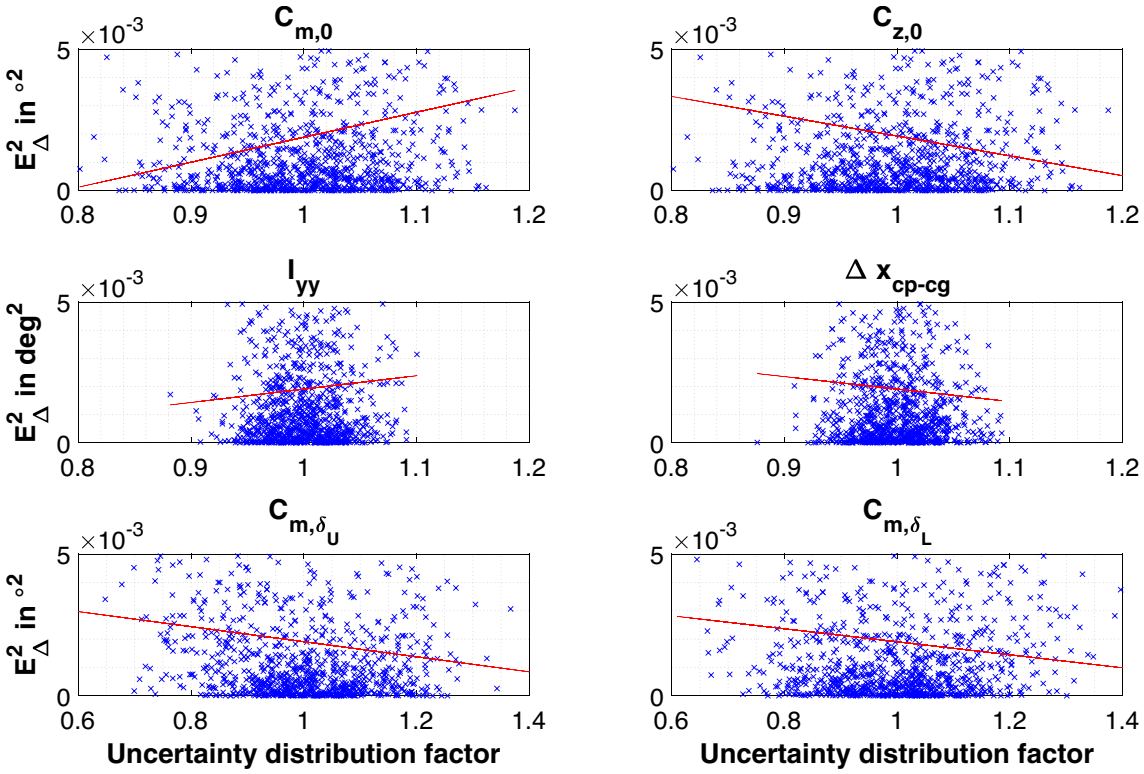

Fig. 20 Simulation results for E_Δ^2 each simulation sample plotted over the uncertainty spreading of each defined uncertain parameter at S_3 at $T = 8.83$

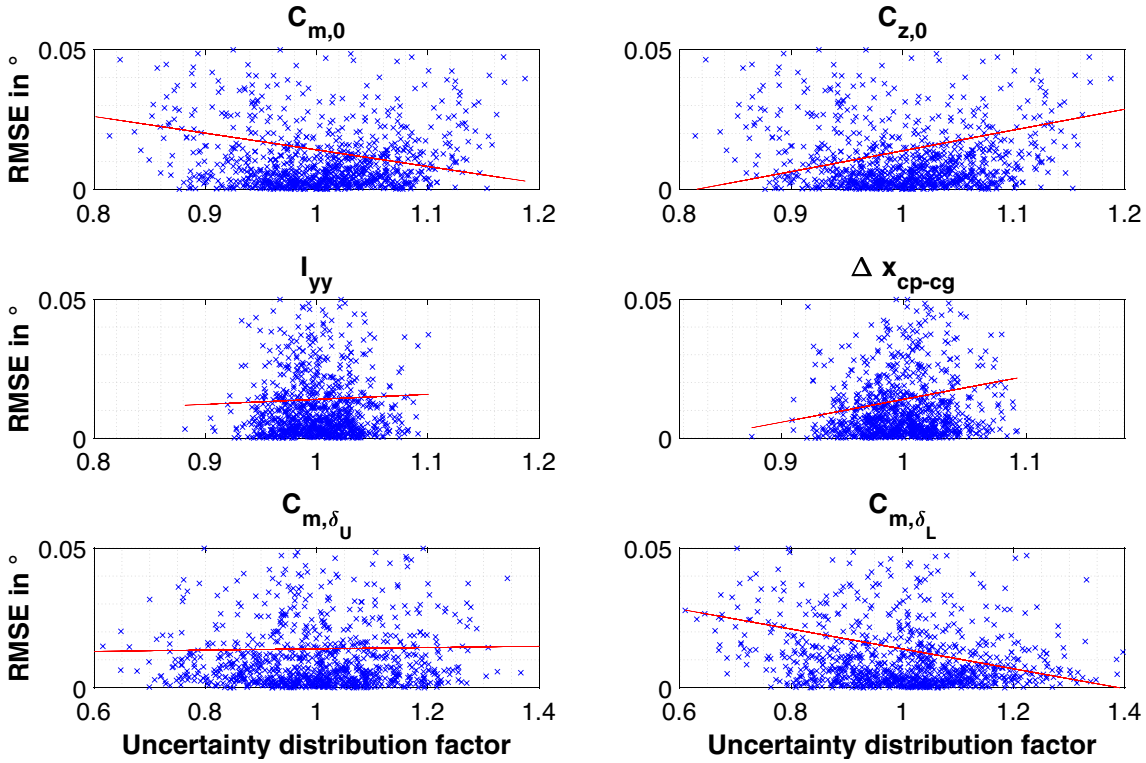

Fig. 21 Simulation results for the root mean square error between the nominal value and the observed closed-loop response each simulation sample plotted over the uncertainty spreading of each defined uncertain parameter

response can be identified for n_z and the lower flaps $C_{m,\delta_L L}$ and $C_{m,\delta_L R}$. The increased influences of the lower flaps can be explained by the fact that they have a higher control effectiveness in the regarded flight state with the regarded upward manoeuvre. Hence, a movement on them contributes more beneficial to the balance of moment. The negative slope of the linear fit for the flaps with increasing uncertainty distribution factor can be explained by the increased influence on the error cancellation of the controller. Due to that the integrators do not need to integrate for that long to lower the tracking error; hence, an uncertainty factor > 1 for the lower flaps is beneficial. The signs of the slope for $C_{z,0}$ and Δx_{cp-cg} need to be similar since both are contributing in the same way on the balance of moment via the cross product. Figure 20 shows the results for S_3 at $T = 8.83$. The plots indicate that again $C_{m,0}$, $C_{z,0}$, Δx_{cp-cg} and C_{m,δ_L} have bigger influences on E^2_Δ. Additionally, now also C_{m,δ_U} has an similar influence on E^2_Δ as C_{m,δ_L}. The sign of the slopes has changed for all linear fits but the one for the lower flaps. This makes sense for the parameters $C_{m,0}$, $C_{z,0}$ and Δx_{cp-cg} since their contribution stays the same and hence their influences on E^2_Δ are changing with regards to the downward manoeuvre.

Since it is difficult to compare the influences of the uncertainties at the different time sections, it was decided to also look into the root mean square error between the nominal value and the observed closed-loop response of each simulation sample over the entire time series. The results can be seen in Fig. 21. The parameters that have been identified previously are again dominant, which shows that it would be of interest to address the influences of the uncertainties in the flight control design. This can be, for example, done using an incremental control strategy, as presented in [15]. However, this would only allow to substitute missing model knowledge of $C_{m,0}$, $C_{z,0}$ and Δx_{cp-cg} with sensor-information or estimates. The influences of C_{m,δ_L} would not be addressed. A further option would be to use an adaptive control methodology, such as presented in [51], to ensure an online adaptation concerning possible mismatches. Finally, it would be also possible to use an $\mathcal{H}_\infty$-based robust control approach, such as presented in [52], to ensure that a particular worst-case performance is not undercut.

6 Conclusions

This paper proposes a non-linear model following control architecture for the attitude control of an over-actuated conceptual hypersonic glide vehicle developed by DLR. The core of the suggested control strategy relies on a non-linear

dynamic inversion control methodology for feedback control, which is further extended with a feedforward path based on the idea of non-linear model following control. The control architecture allows the partial separation of the command tracking tasks from the regulation tasks of the feedback control system, which could consequently decrease the possibility of high-gain solutions. To validate the proposed fight control architecture, a set of simulation cases were investigated in Sect. 5. The obtained results suggest that the NMFC is capable of tracking the demanded reference commands for longitudinal and lateral-directional manoeuvres in the nominal, as well as in the presence of specified classes of control effector failures and parametric uncertainties, which implies the robustness of the controller concept.

7 Future work

Future work intends to deeper understand the properties of the proposed NMFC with considering the control of the GHGV-2. An extended robustness analysis will be needed to validate the presented control concept comprehensively. This can be achieved by creating a simulation framework that is able to consider the following points:

- external disturbances, such as atmospheric disturbances
- corrupted sensor signals, such as noise and delayed sensors
- delayed and non-linear actuator dynamics

The findings of Sect. 5 suggest that an enhancement, of the proposed NMFC, might be needed to address the negative effects of model uncertainties. Concepts of adaptive and robust control are currently studied and are planned to be used to robustify the overall control architecture. The proposed controller is currently further evaluated concerning its performance in connection with developed guidance systems. This helps to better understand the inner loop control performance with regard to the overall mission performance. The findings from such an extended performance assessment will demand further design iterations and some fine-tuning on the overall control structure.

Acknowledgements The authors would like to thank and acknowledge all colleagues from DLR working within the HyBAB study for their contributions to the multidisciplinary design of the discussed vehicle. Special thanks go to Dr. Patrick Gruhn from the DLR Institute of Aerodynamics and Flow Technology for helpful discussions and for supporting the vehicle's high-fidelity modeling.

Funding Open Access funding enabled and organized by Projekt DEAL.

Declarations

Conflict of interest All authors declare that they have no conflicts of interest.

References

1. Flight dynamics—Concepts, quantities and symbols—Part 1: Aircraft motion relative to the air. Standard, International Organization for Standardization (ISO), Geneva, Switzerland (April 1988). ISO 1151-1:1988
2. Flight dynamics – Concepts, quantities and symbols – Part 2: Motions of the aircraft and the atmosphere relative to the Earth. Standard, International Organization for Standardization (ISO), Geneva, Switzerland (September 1985). ISO 1151-2:1985
3. Slayer, K.M.: Hypersonic weapons: Background and issues for congress. Technical report, Congressional Research Service (2023). https://crsreports.congress.gov/product/pdf/R/R45811/35
4. Göge, D., Zimper, D., Besser, H., Huggins, M., Alan, S.: Hypersonic vehicles - Game changers for future warfare? Transforming Joint Air Power: The Journal of the JAPCC (2017) https://elib.dlr.de/113912/
5. da Costa, R.R., Chu, Q.P., Mulder, J.A.: Reentry flight controller design using nonlinear dynamic inversion. J. Spacecraft Rockets **40**(1), 64–71 (2003). https://doi.org/10.2514/2.3916
6. Snell, S.A., Enns, F.D., Garrard, W.L.: Nonlinear inversion flight control for a supermaneuverable aircraft. J. Guidance Control Dyn. **15**(4), 976–984 (1992). https://doi.org/10.2514/3.20932
7. Tipàn, S., Theodoulis, S., Thai, S., Proff, M.: Nonlinear dynamic inversion flight control design for guided projectiles. J. Guidance Control Dyn. **43**(5), 975–980 (2020). https://doi.org/10.2514/1.G004976
8. Menon, P.K., Iragavarapu, V., Ohlmeyer, E.: Nonlinear missile autopilot design using time-scale separation. (1997). https://doi.org/10.2514/6.1997-3765
9. Lee, H., Reiman, S., Dillon, C., Youssef, H.: Robust nonlinear dynamic inversion control for a hypersonic cruise vehicle. In: AIAA Guidance, Navigation and Control Conference and Exhibit. https://doi.org/10.2514/6.2007-6685
10. Acquatella, P., Falkena, W., van Kampen, E.-J., Chu, Q.P.: Robust nonlinear spacecraft attitude control using incremental nonlinear dynamic inversion. In: AIAA Guidance, Navigation, and Control Conference (2012). https://doi.org/10.2514/6.2012-4623
11. Pfeifle, O., Fichter, W.: Cascaded incremental nonlinear dynamic inversion for three-dimensional spline-tracking with wind compensation. J. Guidance Control Dyn. **44**(8), 1559–1571 (2021). https://doi.org/10.2514/1.G005785
12. Zhang, J., Wang, J., Zhang, F., Holzapfel, F.: Modeling and Incremental Nonlinear Dynamic Inversion Control for a Highly Redundant Flight System. https://doi.org/10.2514/6.2019-1922
13. Pineau, S., Theodoulis, S., Zasadzinski, M., Boutayeb, M.: Autopilot design for dual-spin projectiles using incremental nonlinear

dynamic inversion. In: 2022 30th Mediterranean Conference on Control and Automation (MED), pp. 444–449 (2022). https://doi.org/10.1109/MED54222.2022.9837217
14. Steffensen, R., Steinert, A., Mbikayi, Z., Raab, S., Angelov, J., Holzapfel, F.: Filter and sensor delay synchronization in incremental flight control laws. Aerospace Syst. **6**, 1–20 (2023). https://doi.org/10.1007/s42401-022-00186-2
15. Autenrieb, J.: Data fusion-based Incremental Nonlinear Model Following Control Design for a Hypersonic Waverider Configuration. https://doi.org/10.2514/6.2023-1997. https://arc.aiaa.org/doi/abs/10.2514/6.2023-1997
16. Jiali, Y., Jihong, Z.: An angular acceleration estimation method based on the complementary filter theory. In: 2016 IEEE International Instrumentation and Measurement Technology Conference Proceedings, pp. 1–6 (2016). https://doi.org/10.1109/I2MTC.2016.7520548
17. Li, Y., Liu, X., He, Q., Ming, R., Huang, W., Zhang, W.: L1 adaptive structure-based nonlinear dynamic inversion control for aircraft with center of gravity variations. J. Intell. Robot. Syst. **106** (2022). https://doi.org/10.1007/s10846-022-01691-4
18. Leitao, M., Peter, F., Holzapfel, F.: Adaptive augmentation of a fighter aircraft autopilot using a nonlinear reference model. In: Proceedings of the 2013 CEAS Specialist Conference on Guidance, Navigation and Control (EuroGNC), Delft, Netherlands (2013)
19. Duda, H., Bouwer, G., Bauschat, J.-M., Hahn, K.-U.: A model following control approach, pp. 116–124 (2007). https://doi.org/10.1007/BFb0113855
20. Gruhn, P.: Design and Analysis of a Hypersonic Glide Vehicle (Original German Title: Auslegung und Analyse Eines Hypersonischen Gleitflugkörpers). In: Conference on Applied Research for Defense and Security in Germany, Bonn, Germany (2020)
21. Chai, R., Tsourdos, A., Savvaris, A., Chai, S., Xia, Y.: Trajectory planning for hypersonic reentry vehicle satisfying deterministic and probabilistic constraints. Acta Astronautica 177, 30–38 (2020). https://doi.org/10.1016/j.actaastro.2020.06.051
22. Autenrieb, J.: Data fusion-based Incremental Nonlinear Model Following Control Design for a Hypersonic Waverider Configuration. https://doi.org/10.2514/6.2023-1997
23. Gerhold, T.: Overview of the hybrid rans code tau. Notes on Numerical Fluid Mechanics and Multidisciplinary Design **89** (2002). https://doi.org/10.1007/3-540-32382-1_5
24. Autenrieb, J., Fezans, N., Gruhn, P., Klevanski, J.: Towards a Control-Centric Modelling and Simulation-Framework for Hypersonic Glide Vehicles. In: German Aeronautics and Space Congress (DLRK), Bremen, Germany (2021). https://doi.org/10.25967/550235
25. Young, T.: International Standard Atmosphere (ISA) Table, pp. 583–590 (2017). https://doi.org/10.1002/9781118534786.app1
26. Fezans, N., Alazard, D., Imbert, N., Carpentier, B.: Robust LPV Control Design for a RLV During Reentry (2010). https://doi.org/10.2514/6.2010-8194
27. Kiehn, D.: Stability analysis and flight control design of the winged reusable launch vehicle ReFEx. CEAS Space J. **13**, 51–64 (2020). https://doi.org/10.1007/s12567-020-00319-3
28. Bolender, M., Doman, D.: Nonlinear Longitudinal Dynamical Model of an Air-Breathing Hypersonic Vehicle. J. Spacecraft Rockets **44**, 374–387 (2007). https://doi.org/10.2514/1.23370
29. Breitsamter, C., Cvrlje, T., Laschka, B., Heller, M., Sachs, G.: Lateral-directional coupling and unsteady aerodynamic effects of hypersonic vehicles. J. Spacecraft Rockets **38**(2), 159–167 (2001). https://doi.org/10.2514/2.3689
30. Acquatella, P., Kampen, E.-J.V., Chu, Q.P.: A Sampled-Data Form of Incremental Nonlinear Dynamic Inversion for Spacecraft Attitude Control. https://doi.org/10.2514/6.2022-0761
31. Holzapfel, F.: Nonlinear adaptive control of an unmanned aerial vehicle (Original German Title: Nichtlineare adaptive regelung eines unbemannten fluggerätes). PhD thesis, Technische Universität München, München, Germany (June 2004). https://mediatum.ub.tum.de/?id=601905
32. Lombaerts, T., Looye, G.: Design and flight testing of nonlinear autoflight control laws. (2012). https://doi.org/10.2514/6.2012-4982
33. Härkegård, O.: Backstepping and control allocation with applications to flight control. PhD thesis, Linköpings universitet, Linköping, Sweden (April 2003). http://www.diva-portal.org/smash/get/diva2:243491/FULLTEXT01.pdf
34. Bordignon, K.A.: Constrained control allocation for systems with redundant control effectors. PhD thesis, Virginia Polytechnic Institute and State University (1996)
35. Durham, W., Bordignon, K., Beck, R.: Aircraft Control Allocation (2016). https://doi.org/10.1002/9781118827789
36. Durham, W.C.: Constrained control allocation. J. Guidance Control Dyn. **16**(4), 717–725 (1993). https://doi.org/10.2514/3.21072
37. Ikeda, Y., Hood, M.: An application of L1 optimization to control allocation. https://doi.org/10.2514/6.2000-4566
38. Bolender, M.A., Doman, D.B.: Nonlinear control allocation using piecewise linear functions. J. Guidance Control Dyn. **27**(6), 1017–1027 (2004). https://doi.org/10.2514/1.9546
39. Huang, X., Duan, G.: Dynamic infinity-norm constrained control allocation for attitude tracking control of overactuated combined spacecraft. IET Control Theory & Applications **13** (2019). https://doi.org/10.1049/iet-cta.2018.5707
40. Bodson, M., Frost, S.A.: Load balancing in control allocation. J. Guidance Control Dyn. **34**(2), 380–387 (2011). https://doi.org/10.2514/1.51952
41. Petersen, J.A.M., Bodson, M.: Interior-point algorithms for control allocation. J. Guidance Control Dyn. **28**(3), 471–480 (2005). https://doi.org/10.2514/1.5937
42. Johansen, T.A., Fossen, T.I., Berge, S.P.: Constrained nonlinear control allocation with singularity avoidance using sequential quadratic programming. IEEE Trans. Control Syst. Technol. **12**(1), 211–216 (2004). https://doi.org/10.1109/TCST.2003.821952
43. Härkegård, O.: Dynamic control allocation using constrained quadratic programming. J. Guidance Control Dyn. **27(6)** (2004). https://doi.org/10.2514/1.11607
44. Stellato, B., Banjac, G., Goulart, P., Bemporad, A., Boyd, S.: OSQP: an operator splitting solver for quadratic programs. Math. Programming Comput. **12**(4), 637–672 (2020). https://doi.org/10.1007/s12532-020-00179-2
45. Lombaerts, T., Looye, G., Chu, P., Mulder, J.A.: Pseudo Control Hedging and its Application for Safe Flight Envelope Protection. https://doi.org/10.2514/6.2010-8280
46. Johnson, E.N., Calise, A.J.: Pseudo-control hedging: A new method for adaptive control. In: Advances in Navigation Guidance and Control Technology Workshop, pp. 1–2 (2000). Alabama, USA Alabama, USA
47. Holzapfel, F., Sachs, G.: Dynamic inversion based control concept with application to an unmanned aerial vehicle. In: AIAA Guidance, Navigation, and Control Conference and Exhibit, p. 4907 (2004). https://doi.org/10.2514/6.2004-4907
48. van 't Veld, R., Kampen, E.-J.V., Chu, Q.P.: Stability and Robustness Analysis and Improvements for Incremental Nonlinear Dynamic Inversion Control. https://doi.org/10.2514/6.2018-1127
49. Padula, F., Visioli, A., Pagnoni, M.: On the anti-windup schemes for fractional-order pid controllers. In: Proceedings of 2012 IEEE 17th International Conference on Emerging Technologies & Factory Automation (ETFA 2012), pp. 1–4 (2012). https://doi.org/10.1109/ETFA.2012.6489758
50. Wang, J., Bierling, T., Höcht, L., Holzapfel, F., Klose, S., Knoll, A.: Novel Dynamic Inversion Architecture Design for Quadrocopter Control, pp. 261–272 (2011). https://doi.org/10.1007/978-3-642-19817-5_21

51. Famularo, D.I., Valasek, J., Muse, J.A., Bolender, M.A.: Adaptive Control of Hypersonic Vehicles Using Observer-Based Nonlinear Dynamic Inversion. https://doi.org/10.2514/6.2018-0843. https://arc.aiaa.org/doi/abs/10.2514/6.2018-0843
52. Liu, H., Liu, D., Xi, J., Yu, Y.: Robust control for hypersonic vehicles with parametric and unstructured uncertainties. Proc. Inst. Mech. Eng. Part C **232**(13), 2369–2380 (2018). https://doi.org/10.1177/0954406217720821